ABSTRACT

Title of Document: A GEOCHEMICAL AND OSMIUM ISOTOPIC STUDY OF THE GROUP IVB IRONS AND UNGROUPED IRONS CHINGA, TISHOMINGO AND WILLOW GROVE
Jenise Marie Honesto, M.S., 2006

Directed By: Professor William F. McDonough, Department of Geology

Re-Os isotopic and highly siderophile element (HSE) systematics of IVB irons and ungrouped iron meteorites Chinga, Tishomingo and Willow Grove are presented. IVB iron composition has been constrained by HSE (Re, Os, Ru, Ir, Pt, and Pd) abundances, showing a limited range of Pt concentration (31.15 to 32.75 ppb) despite a wide range in nickel (Ni) content (15.64 to 18.02 wt %). Using the Re-Os system, a crystallization age of 4575 ± 56 Ma was determined for the group. Fractional crystallization modeling suggests these samples crystallized from a non-chondritic parent-body. Chinga is shown to be unrelated to the IVBs through HSE abundances, and fractional crystallization modeling. Willow Grove and Tishomingo have HSE patterns comparable to the IVBs. Tishomingo has a platinum concentration within the range of the IVBs. The high Ni content of these two irons (>27 wt %) poses a problem for their formation by simple fractional crystallization.

A GEOCHEMICAL AND OSMIUM ISOTOPIC STUDY OF THE GROUP IVB IRON METEORITES AND UNGROUPED IRONS CHINGA, TISHOMINGO AND WILLOW GROVE

By

Jenise Marie Honesto

Thesis Submitted to the Faculty of the Graduate School of the
University of Maryland, College Park in partial fulfillment
of the requirements for the degree of
Master of Science
2006

Advisory Committee:
Professor W.F. McDonough, Chair
Professor A.J. Campbell
Professor R.J. Walker

Dedication

To grandpa, who never quite understood my desire to study rocks or to leave California, but who wore his Maryland shirt each week. I started this project with him, and although I complete it without him, I know he is proud.

and

To Matt, who knew exactly what to say to make the last few months fly by faster than either of us could have hoped. I started this project without him, but I finish it with his endless love and support, and that has made all the difference.

Acknowledgements

First and foremost, I would like to acknowledge my fellow graduate students who have shared in the ups and downs of the last two years, and who have made the ups enjoyable and the downs bearable. Barry Reno and Tom Ireland were especially helpful having been my faithful and most trusted friends since I arrived at Maryland. Special thanks to my office mates, Tracey Centorbi, Ricardo Arevalo, and especially Fang-Zhen Teng, for providing the everyday humor necessary to make the days seem shorter. Nick Geboy, Melissa Wilmot, John Jamieson and Sean Timpa were also instrumental to the completion of this thesis and to the maintenance of my sanity.

The professors of the department deserve to be acknowledged for the many interesting discussions often provoked by their teaching or laboratory work. Special thanks to my committee, Bill McDonough, Rich Walker and Andy Campbell, for the dedication of their time and patience to the completion of this thesis. I have also had the additional guidance of my collaborators that I have had the pleasure to work with over the past two years, especially Tim McCoy and Cari Corrigan. And finally, Richard Ash, whose assistance and humor both in and out of the lab have been much appreciated during the course of my work.

I also would never have been able to navigate the Maryland world without the skillful guidance and sound direction of the professional staff. I'd like to thank Sandy Romeo for the always thoughtful conversations, Roz Pinkard for her care, concern, and wonderful sense of humor, and Jeanne Martin, whose endless knowledge of all things Maryland is greatly appreciated.

I did not get to Maryland alone, but it was with the support and encouragement of my parents, brothers and extended family, whom I left in California to pursue this work. My older brother, Gabe, is in need of special thanks for all the times I woke him with an early morning phone call because I needed to talk to someone and didn't want to make our parents worry. I never would have survived that first semester had it not been for his ability to reassure me over the phone while trying not to fall back to sleep.

Table of Contents

1. Introduction

For many years, meteorites have been the subject of intense study in order to determine their composition, as well as to gain insight into processes that may have occurred in the early solar system. Meteorites can be divided into two groups: undifferentiated, or primitive meteorites, and differentiated meteorites.

1.1 Differentiated Meteorites

Differentiated meteorites are parts of a planet or planetesimal that was segregated into a core, mantle and crust. Highly focused studies of the elemental and isotopic systematics of groups of differentiated meteorites can be used to constrain the formation of these different parts of planets.

Differentiated meteorites are divided into several groups, whose only shared characteristic is the segregation of metal from silicate. The three subdivisions of differentiated samples are achondrites, stony-irons and irons. Achondrites, as their name implies, lack chondrules. They resemble terrestrial igneous rocks and their texture serves as evidence of igneous processes that have differentiated these rocks from the chondritic protolith. Achondrites are further grouped based on compositional and textural features and include lunar and Martian meteorites. Stony-irons are samples that have both defined metal and silicate domains. Within the stony-iron classification are two subsets: pallasites and mesosiderites. Pallasites are composed of olivine crystals enclosed in an iron-nickel alloy matrix and are believed to be samples taken from the core-mantle transition zone of differentiated bodies. Mesosiderites are a brecciated mixture of iron and silicate in near equal quantities and thought to be the remnant of repeated impacts altering the parent-body. Although chondrites, achondrites and stony-irons are all

fascinating samples for study in their own right, this study is focused on the iron meteorites.

1.2 Iron Meteorites

Of the differentiated meteorites, irons are of particular interest because of their metal-rich composition and lack of large-scale inclusions. There is only one terrestrial rock that closely resembles iron meteorites, josephinites, a deep-mantle derivative (BIRD and WEATHERS, 1979). The origins of iron meteorites have been postulated to be samples of asteroidal cores or the result of iron segregation that formed as a result of impact processes (BUCHWALD, 1975; SCHAUDY et al., 1972; WASSON et al., 1980). Iron meteorites are composed primarily of an iron-nickel alloy, with mineralogy of primarily taenite ($Fe_{0.8}Ni_{0.2}$) and kamacite ($Fe_{0.9}Ni_{0.1}$). In some cases, taenite can be transformed at low temperatures to martensite, a low temperature iron-nickel alloy. The intergrowth of taenite and kamacite occurs as the core solidified and results in a Widmanstätten pattern or, in the case of a finer intermixture, plessite.

Within iron meteorites it is possible to observe accessory phases, such as the phosphide, schriebersite [$(Fe, Ni)_3P$], and the sulfide, troilite (FeS). Schreibersite is especially important because of the structural link to the nucleation and growth of kamacite crystals (RASMUSSEN et al., 1984). Inclusions of daubreelite ($FeCr_2S_4$) have been observed in some irons as well. The size and number of inclusions varies by iron group, with some groups having numerous but small inclusions and others having fewer in number but larger in size inclusions. Some irons have very few, very small silicate inclusions. Unlike chondrites, which have abundant silicate and oxides grains, these types of inclusions are not as common in iron meteorites.

Iron meteorites, like almost all rocks, are classified on the basis of structural and compositional characteristics. Classifications initially based on texture alone were later coupled with compositional classifications (LOVERING et al., 1957; SCHAUDY et al., 1972; WASSON, 1974). One of the first classification schemes for iron meteorites developed by Lovering et al. (1957) utilized the concentrations of gallium, germanium and nickel in each sample. By observing the concentration of Ga and Ge, two volatile elements, four iron meteorite groups were determined and labeled I, II, III and IV corresponding to decreased concentration (LOVERING et al., 1957). As these groupings were further explored, and other elemental concentrations were determined, letters were added to distinguish the observed chemical groupings of the expanded elemental dataset (Figure 1). Each iron group is believed to represent a distinctive planetary core of a failed planetesimal or other segregated metallic body (BUCHWALD, 1975; WASSON, 1985; WASSON et al., 1980).

Some irons are chemically distinct relative to previously documented groups. Such irons are classified as either an anomalous member of an existing group, such as Chinga grouped with the IVB irons (SCHAUDY et al., 1972), or as ungrouped, as is the case for Tishomingo and Willow Grove (BIRCH et al., 2001). The former classification is only implemented if there is substantial evidence to suggest compositional link between the iron and the group. The latter classification is more commonly used for irons that are not easily chemically linked to a group.

There have been a wide variety of studies of irons. Some have determined the cooling history of iron meteorite groups, including the resolution of diverse metallographic cooling rates with constrained chemical trends in the IVA group (HAACK

et al., 1996). Other studies of cooling history have explored the pressure-temperature conditions in the nebula assuming equilibrium condensation for a variety of iron groups (SEARS, 1978) and impact and cooling history of non-magmatic irons (WASSON and KALLEMEYN, 2002). Inferred parent body processes and meteorite composition has also been studied, initially to classify and group irons (SCHAUDY et al., 1972; SCOTT et al., 1996), and more recently to constrain groups, determine ages and postulate parent-body processes (CAMPBELL and HUMAYUN, 2005; COOK et al., 2004; RASMUSSEN et al., 1984; SHEN et al., 1996; SMOLIAR et al., 1996). Of these, the work by Campbell and Humayun (2005) is a recent, highly focused study of IVB irons.

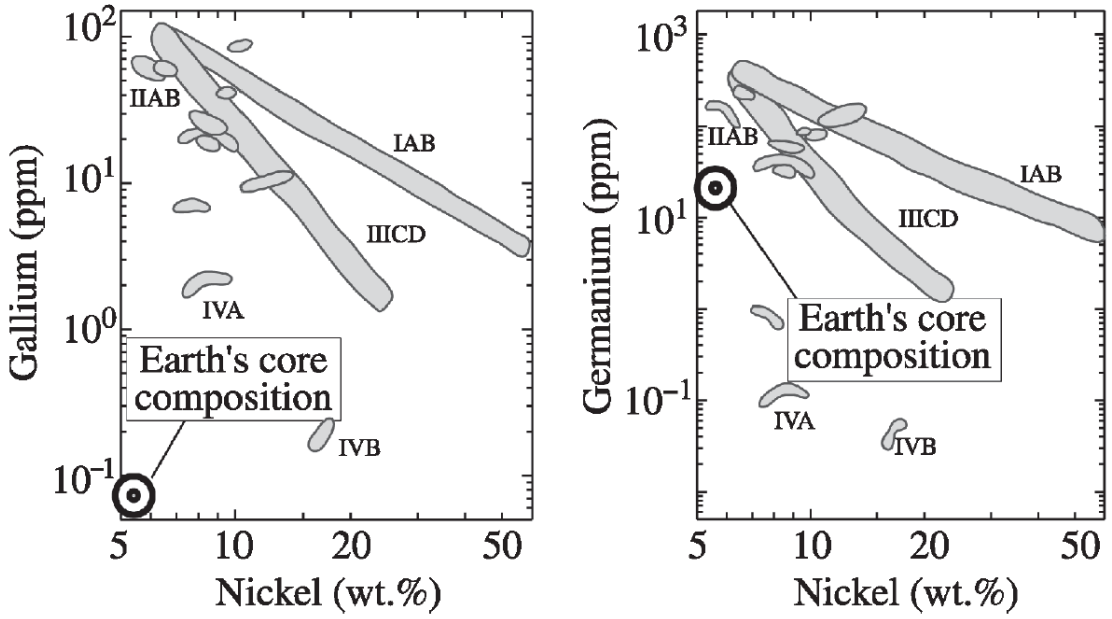

Figure 1: Illustration of iron meteorite groups as defined by concentration of Ga (left) and Ge (right) v. Ni (wt%). Note IVB irons plot significantly below most iron groups with respect to Ga and Ge, but have a restricted range of Ni concentration. From (MCDONOUGH, 2003), after Wasson (1985).

This study focuses on the group IVB iron meteorites, two ungrouped and one anomalous iron (Tishomingo, Willow Grove and Chinga, respectively) which exhibit

some compositional similarities to the IVB group. The IVB group is limited to only 12 members; the limited number of samples has been attributed to insufficient sampling by the Earth when compared to the larger iron meteorite groups (RASMUSSEN et al., 1984). The size of the group does not diminish the compositional features of the member meteorites that define the structure and composition of the group. Most notable of these compositional features are high concentrations of Ni, depletion in volatile elements, specifically Ga and Ge, and enrichment in the highly siderophile elements (HSE) Re, Os, Ir, Ru, Pt and Pd (Table 2). The high weight percent nickel (~16 to 18 wt %) of the IVB group makes the ungrouped irons Tishomingo and Willow Grove suitable for comparison to the group, as these irons have high Ni contents (>28 wt %). Chinga is of interest because it was initially classified as an anomalous member of the IVB group (SCHAUDY et al., 1972; WASSON, 1974) and then later as an ungrouped iron (RASMUSSEN et al., 1984). Comparison of Chinga to the IVB irons is proposed because Chinga has a comparable nickel concentration, however, it has a much lower concentration of highly siderophile elements. Further study of the IVB group and Chinga will better define the relationship, if any, between these irons.

Texturally, both IVB irons and the ungrouped irons of interest fall within the structural category D, or ataxite, which is noted for having Ni concentrations greater than 16 weight percent (Table 1; (MITTLEFEHLDT et al., 1998). Ataxite literally means lacking structure, so the IVB and ungrouped irons all lack macroscopic scale intergrowth of taenite and kamacite. Another characteristic of the ataxites are the appearance of up to centimeter-wide diffuse bands in etched sections. While all IVB irons are ataxites, not all ataxites are IVB irons, as ungrouped irons such as Washington County and Nedagolla, as

well as some Group IIF irons, are ataxites but are genetically unrelated to the IVB group (BUCHWALD, 1975).

Table 1: Structural Classification of Iron Meteorites

Structural Class	Symbol	Kamacite bandwidth (mm)	Nickel (wt %)	Chemical Groups
Hexahedrites	H	>50	4.5 - 6.5	IIAB, IIG
Coarsest Octahedrites	Ogg	3.3 - 50	6.5 - 7.2	IIAB, IIG
Coarse Octahedrites	Ogg	1.3 - 3.3	6.5 - 8.5	IAB, IC, IIE, IIIAB, IIIE
Medium octahedrites	Om	0.5 - 1.3	7.4 - 10	IAB, IID, IIE, IIIAB, IIIF
Fine octahedrites	Of	0.2 - 0.5	7.8 - 13	IID, IIICD, IIIF, IVA
Finest octahedrites	Off	<0.2	7.8 - 13	IIC, IIICD
Plessitic octahedrites	Opl	<0.2, spindles	9.2 - 18	IIC, IIF
Ataxites	D	-	>16	IIF, ***IVB***

1.3 Scope of Present Study

This study examines eleven of the twelve members of the group IVB iron meteorites, the ungrouped irons Tishomingo and Willow Grove, and the anomalous Chinga. These samples have been studied to determine highly siderophile element (HSE) and osmium isotope systematics of the IVB group, as well as to use the constrained composition of the group to explore possible relationships between the IVB irons and the ungrouped irons of interest. The systematics employed herein to explore the potential genetic relationship is three-fold: first, to examine the highly siderophile element composition, second, to determine the crystallization age and demonstrate closed-system behavior of the irons using the Re-Os isotope system, and third, to investigate the formation of the group IVB irons, and the ungrouped irons of interest, using simple fractional crystallization modeling.

2. Background

The distinguishing features of the group include high nickel content (greater than 15 weight percent), high concentration of Ir (>12 ppm) and other HSE, and low Ga and Ge concentrations (less than 0.3 and 0.10 ppm, respectively). The composition of the

IVB irons has been determined from earlier studies (CAMPBELL and HUMAYUN, 2005; RASMUSSEN et al., 1984; SCHAUDY et al., 1972; SCOTT, 1972). In addition to composition, these studies of the IVB irons have also determined elemental fractionation (SCOTT, 1972), cooling rates (RASMUSSEN et al., 1984) and the fractional crystallization processes (CAMPBELL and HUMAYUN, 2005) that formed the group.

2.1 Elemental Fractionation in the IVB Group

Aside from high Ni and Ir concentration and low Ga and Ge, the IVB irons can also be distinguished by the fractionation of elements relative to the concentration of nickel in the sample. Elemental fractionation shows the change in concentration as a function of crystal liquid fractionation. The distribution of certain elements among iron meteorite groups has been explored previously, and the results can be very useful in classifying IVB irons (SCOTT, 1972). Gallium and germanium are two elements from which initial iron meteorite groupings were based (LOVERING et al., 1957), however, Scott (1972) noted that while the range of Ge in all iron groups spans across four orders of magnitude, the fractionation of Ge within an individual group does not exceed a factor of two.

Scott (1972) described the fractionations of other elements in iron meteorite groups. Phosphorous (P) abundances tend to correlate positively with nickel in the IVB group, while also having a limited range of concentration (~0.05 to 0.1 weight percent). Gold (Au) is ten times less concentrated in the IVB group than in the other iron groups. By contrast, palladium (Pd) is highly concentrated in the IVB group compared to other iron groups, and shows that Ni does not vary by much as Pd concentrations become enriched. Molybdenum is also about double the concentration of other iron groups.

Platinum and ruthenium correlate positively with nickel and have higher concentrations than the other iron groups (SCOTT, 1972). With respect to both Re and Os, the IVB group is enriched when compared to the other iron meteorite groups. Nickel and Ir are negatively correlated for the IVB group, however, there is a slight positive correlation in the ungrouped iron Ni-Ir relationship (Figure 2).

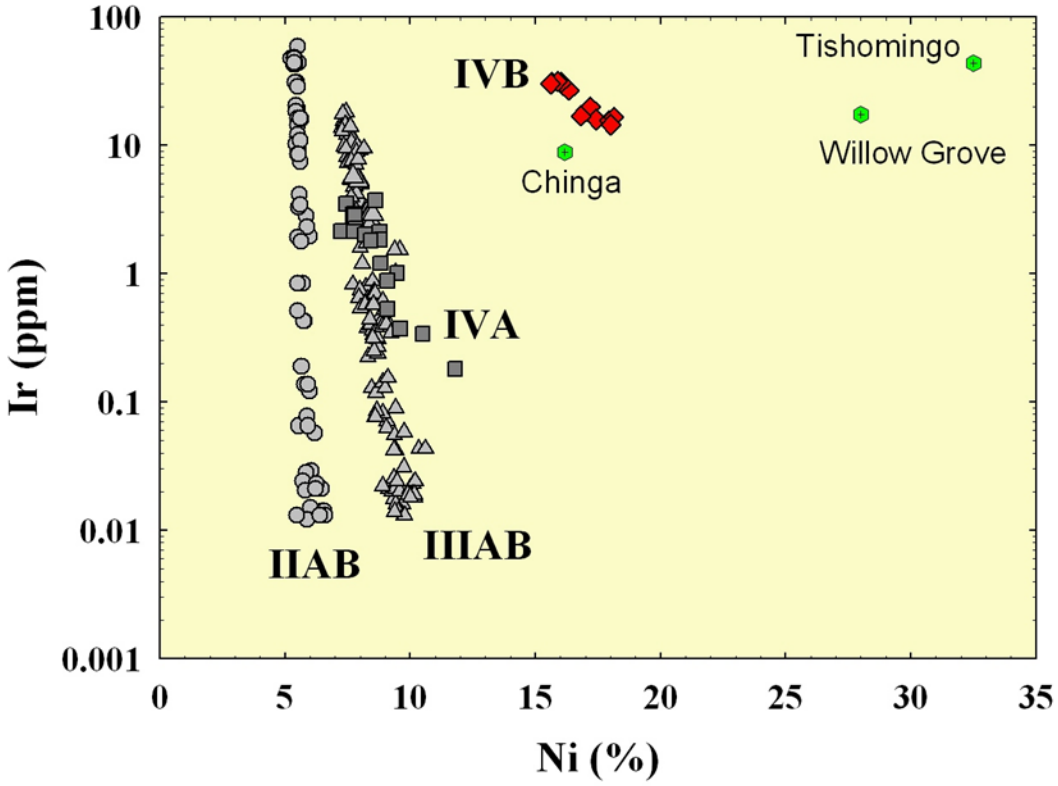

Figure 2: Diagram of Ni (wt%) v. concentration of Ir (ppm) for iron groups and the ungrouped irons of interest. Red diamonds represent IVB irons, green hexagons represent ungrouped irons of interest. Ir data for IVB and ungrouped irons from this study, and from Wasson, 1974 for all other irons. Ni data from Schaudy et al., 1972, Wasson, 1974, Birch et al., 2001, and Campbell and Humayun, 2005.

The IVB group shows a mid-range chromium concentration that is distinguishable from the other groups when plotted versus nickel. The concentration of copper in the IVB group is an order of magnitude lower than the other iron groups. Zinc is also of very

low concentration in the IVB group, however, unlike Cu, the depleted Zn is also a feature of the IIA, IIB, IIE, and the IVA groups (SCOTT, 1972).

2.2 Composition and Origin of the IVB parent body

Rasmussen et al. (1984) studied the compositions of group IVB irons and calculated cooling rates. Volatile abundances were determined to be lower than other iron groups consistent with the significantly depleted Ga and Ge concentrations previously noted by Schaudy et al. (1972). The IVB group also displays significant variations from the chondritic abundance of refractory and volatile elements: the IVB group has triple the concentration of refractory elements, while the volatile elements have been depleted in the IVB irons compared to chondrites. It has been suggested that the volatile depletion may be attributable to planetary outgassing while the enriched refractory elements may be due to oxidation of the parent melt (RASMUSSEN et al., 1984). Outgassing is the slow release of gases from some solid material consequently this process would release elements that prefer the gaseous phase. The oxidation of the parent melt would remove Fe from the core and into the mantle while the remaining melt would become enriched in Ni and other less easily oxidized elements.

Rasmussen and colleagues also estimated the cooling rates for the IVB irons using kamacite spindle growth as a function of cooling. In the IVB irons, schriebersite grains are often found completely surrounded by kamacite spindles, which led to the conclusion that kamacite nucleates from schriebersite (RASMUSSEN et al., 1984). The cooling rate estimations were made by calculating a one-dimensional growth model assuming kamacite growth nucleated from schriebersite (RASMUSSEN et al., 1984). The resulting cooling rate for the IVB irons ranged from 110 to 450 K/Ma and 90 to 260 K/Ma for 0K

and 20K undercooling, respectively. Undercooling is the process by which the temperature of the melt is lowered below any transition temperature while still maintaining the liquid form. Earlier cooling rate studies by Goldstein and Short (1967) determined much lower cooling rates for the IVB irons (2 – 80 K/Ma), but this earlier cooling rate determination was based on 110 K undercooling.

Fractional crystallization modeling uses the composition of these irons to deduce their sequence of crystallization. Topics not covered by the scope of this work include the origin of the parent-body of the modeled irons, and any microstructural changes that occurred after crystallization.

The origin of the IVB parent-body has been explored in a more recent study by Campbell and Humayun (2005). Campbell and Humayun (2005) describe the composition and formation of the IVB irons and the origin of the IVB parent-body using data collected for seven samples from the IVB group. Campbell and Humayun assume the distribution coefficient (D) of each element is independent of the fraction of melt crystallized (*f*) and utilized a log(P)-log(E) plot to simultaneously fit all data while holding D_P to an experimental value. To model fractional crystallization in the IVB with these parameterized D-values Campbell and Humayun (2005) used the Rayleigh equation (1):

$$(1) \qquad C_S = C_O \times D \times (1-f)^{D-1}$$

where C_S is the concentration in the solid of the element of interest, C_O is the concentration in the initial melt, D is the distribution coefficient of the element, and *f* is the fraction of crystallization. The resulting fractional crystallization model is in agreement with the earlier model of Rasmussen et al. (1984) with respect to the range of *f*

values (0.16 to 0.86, and .04 to .92, respectively). This model also determined that the IVB parent melt had a fractionated CI chondrite-normalized composition that was a function of elemental volatility, with the most refractory elements being enriched with respect to Ni and depletions in more volatile elements. Notable depletions in siderophile elements (especially Fe, W and Cr) were also observed in the group, suggesting that redox processes were coupled with volatilization to have some effect on the IVB parent metal-melt composition.

Evidence for the oxidation of the core of the IVB parent body was found in the form of depletions in the ratios of Fe and other elements relative to one another (CAMPBELL and HUMAYUN, 2005). Oxidative loss of Fe could explain the low Fe/Ni and Fe/Pd in these irons. However, since the Ni/Pd ratio remains close to chondritic, oxidation responsible for the changes in Fe/Pd and Fe/Ni would not be able to explain the extreme depletion in Ni as was previously suggested (RASMUSSEN et al., 1984).

Campbell and Humayun (2005) propose a five-step sequence of events to form the IVB parent-body. The first stage of formation is characterized by high temperature volatilization and condensation in the solar nebula. This step fractionates refractory siderophile elements (Mo, Ru, Rh, W, Re, Os, Ir, Pt) in metal grains. The next step involves the accretion of the IVB parent body from the refractory metal. Included in this accretion is Fe-Ni metal that may not have had the refractory siderophiles fractionated from one another. The third step in formation as described is the heating of the IVB parent body to a high internal temperature (<1760 K) and low pressure. This step mixes the metal sources, which in Campbell and Humayun (2005) use to explain the relationship of refractory siderophile element abundances as a function of volatility.

During the process of melting and metal/silicate segregation the oxygen fugacity was approximately IW -1, where IW is the iron-wustite buffer to which oxygen fugacity in a system can be compared. This penultimate step can also explain the high concentration of Ni in the samples by the oxidative loss of up to 28% of the total Fe in the melt. The final step of this proposed sequence is fractional crystallization of the melt. This step encompasses the formation of the IVB irons and covers a temperature range of approximately 1760 to 1700 K.

2.3 Origin and Composition of the Ungrouped Irons

Approximately 15% of all iron meteorites have been classified as ungrouped (SCOTT, 1972). This study has compared a set of three ungrouped irons to the IVB irons. Chinga, Tishomingo and Willow Grove all show a similarity in at least two distinguishing features of the IVB signatures; low Ga and Ge, high Ir and high Ni. In the case of Willow Grove and Tishomingo, the outlier is Ni, whereas the outlier for Chinga is Ir concentration (Tables 2 and 3).

The origin of Tishomingo was explored by Ives and colleagues in 1978, while the origin of Willow Grove has been related to that of Tishomingo by Birch et al. (2001). Tishomingo and Willow Grove both have a martensitic structure. Martensite is the result of diffusionless transformation of face-centered cubic structure taenite, into body-centered cubic structure martensite. If Tishomingo was originally one large taenite crystal as has been suggested by Ives et al. (1978), then the taenite would have formed by slow cooling at elevated temperatures. However, martensite is the result of a significant decrease in temperature to a range between 248 and 208 K. To achieve the 80% martensite observed in Tishomingo, Ives and colleagues noted that this required

additional cooling to 198 to 158 K. Also noted in Tishomingo was the reversion of martensite back to taenite, a phenomenon that can be explained by shock deformation and thermal aging at ~170 kbar of pressure and a temperature in excess of 673 K (IVES et al., 1978). In summary, the origin of Tishomingo as evidenced by the microstructures of the sample has been theorized to involve extreme temperature fluctuation, diffusionless transformation and shock deformation.

TABLE 2: IVB Iron Data from previous studies

Meteorite	Ni wt %	Ga ppm	Ge ppm	Ir ppm	Au ppm	As ppm	W ppm	Re ppm	Cr ppm
Cape of Good Hope[1]	16.92	0.198	0.06	36					
Cape of Good Hope[2]	16.3	0.198	0.060	27.5	0.062	0.28	3.01	3.44	241
Cape of Good Hope[3]	15.64 ± 0.16	0.151 ± 0.009	0.050 ± 0.005	35.4 ± 1.5	0.059 ± 0.002	0.19*	3.49 ± 0.05	3.96 ± 0.10	261 ± 20
Hoba[1]	16.56	0.192	0.047	27					
Hoba[2]	16.4	0.192	0.047	23.2	0.084	0.40	3.2	2.9	179
Hoba[3]	16.33 ± 0.10	0.148 ± 0.011	0.059 ± 0.009	29.0 ± 1.3	0.078 ± 0.003	0.48 ± 0.09	3.25 ± 0.05	3.13 ± 0.04	178 ± 14
Iquique[1]	16.03	0.17	0.051	28					
Iquique[2]	16.0	0.170	0.051	27.1	0.069	0.21	4.72	3.36	275
Kokomo[1]	15.83	0.193	0.032	31					
Kokomo[2]	15.9	0.193	0.032	26	0.068	0.37	3.08	3.18	228
Santa Clara[2]	17.9	0.220	0.054	16.9	0.108	0.76	3.06	1.82	106
Santa Clara[3]	17.19 ± 0.20	0.201 ± 0.012	0.065 ± 0.008	21.8 ± 1.0	0.127 ± 0.004	0.73 ± 0.03	3.42 ± 0.04	2.13 ± 0.03	76 ± 7
Skookum[1]	17.13	0.272	0.057	15					
Skookum[2]	18.0	0.272	0.057	12.8	0.152	1.03	2.92	1.34	15
Skookum[3]	17.43 ± 0.19	0.222 ± 0.014	0.080 ± 0.006	17.0 ± 0.9	0.142 ±0.003	1.03 ± 0.09	3.16 ± 0.07	1.59 ± 0.03	36 ± 3
Tawallah Valley[1]	17.06	0.248	0.068	16					
Tawallah Valley[2]	17.6	0.248	0.068	13.5	0.161	1.04	3.1	1.46	83
Tawallah Valley[3]	17.94 ± 0.24	0.198 ± 0.012	0.075 ± 0.006	16.9 ± 0.9	0.152 ± 0.004	0.89 ± 0.05	3.27 ± 0.10	1.59 ± 0.04	69 ± 5
Ternera^[1]	17.58	0.253	0.063	15					
Ternera[2]	17.8	0.262	0.060	14.4	0.168	1.08	3.04	1.65	72
Ternera[a]	18.13	0.261	0.056	16					
Tlacotepec[1]	15.82	0.195	0.031	20					
Tlacotepec[2]	16.2	0.200	0.031	26.3	0.065	0.34	2.86	3.01	140
Tlacotepec[3]	15.60 ± 0.17	0.156 ± 0.010	0.051 ± 0.005	33.3 ± 1.5	0.059 ± 0.002	0.21 ± 0.04	3.45 ± 0.10	3.66 ± 0.05	159 ± 13
Warburton Range[1]	17.8	0.244	0.064	13					
Warburton Range[2]	18.0	0.244	0.064	12.4	0.166	1.08	3.27	1.18	70
Warburton Range[3]	18.02 ± 0.32	0.225 ± 0.014	0.100 ± 0.007	16.4 ± 0.7	0.174 ± 0.004	0.88 ± 0.05	3.77 ± 0.12	1.52 ± 0.03	76 ± 6
Weaver Mountains[1]	16.81	0.233	0.058	17					
Weaver Mountains[2]	17.7	0.257	0.058	14.6	0.129	0.91	2.98	1.46	96
Chinga#[1]	16.18	0.181	0.082	3.6					
Chinga#[2]	16.5	0.181	0.082	3.9	0.51	1.76	0.61	0.96	890

[a] From Wasson, 1974
[1] From Schaudy et al., 1972
[2] From Rasmussen et al., 1984
[3] From Campbell and Humayun, 2005
^ Gallegos, part of Ternera
# Listed as anomalous member of IVB group
* Detection limit

TABLE 2: IVB Iron Data from previous studies, continued

Meteorite	Co ppm	Cu ppm	P ppm	V ppm	Os ppm	Pt ppm	Mo ppm	Ru ppm	Rh ppm	Pd ppm
Cape of Good Hope[1]										
Cape of Good Hope[2]	7660									
Cape of Good Hope[3]	7820 ± 30	1.48 ± 0.06	445 ± 13	0.95 ± 0.04	55.0 ± 1.5	29.6 ± 1.2	25 ± 2	31.4 ± 0.7	4.87 ± 0.11	6.10 ± 0.17
Hoba[1]										
Hoba[2]	7580									
Hoba[3]	7807 ± 14	1.62 ± 0.07	757 ± 27	1.08 ± 0.34	41.9 ± 1.3	28.6 ± 1.2	26 ± 2	28.5 ± 0.6	4.81 ± 0.10	6.67 ± 0.11
Iquique[1]										
Iquique[2]	7420									
Kokomo[1]										
Kokomo[2]	7620									
Santa Clara[2]	7910									
Santa Clara[3]	7797 ± 55	1.54 ± 0.06	1250 ± 113	0.05 ± 0.01	25.9 ± 0.8	30.0 ± 1.3	33 ± 2	25.5 ± 0.7	5.06 ± 0.13	9.01 ± 0.27
Skookum[1]										
Skookum[2]	7520									
Skookum[3]	7912 ± 55	1.89 ± 0.02	2019 ± 469	0.37 ± 0.08	18.7 ± 0.7	28.4 ± 1.3	37 ± 3	23.2 ± 0.9	4.84 ± 0.16	9.88 ± 0.26
Tawallah Valley[1]										
Tawallah Valley[2]	7900									
Tawallah Valley[3]	8158 ± 41	1.87 ± 0.05	1762 ± 377	0.09 ± 0.01	18.3 ± 0.7	29.9 ± 1.4	37 ± 3	23.0 ± 0.9	4.97 ± 0.18	10.71 ± 0.23
Ternera^[1]										
Ternera[2]	7840									
Ternera[a]										
Tlacotepec[1]										
Tlacotepec[2]	7600									
Tlacotepec[3]	7687 ± 90	1.29 ± 0.03	472 ± 18	0.37 ± 0.04	50.6 ± 1.5	29.0 ± 1.2	25 ± 2	29.9 ± 0.7	4.82 ± 0.11	6.38 ± 0.16
Warburton Range[1]										
Warburton Range[2]	7980									
Warburton Range[3]	8021 ± 47	2.08 ± 0.05	1950 ± 206	0.22 ± 0.03	17.4 ± 0.5	31.1± 1.2	42 ± 3	23.8 ± 0.6	5.23 ± 0.11	11.34 ± 0.24
Weaver Mountains[1]										
Weaver Mountains[2]	7940									
Chinga#[1]										
Chinga#[2]	5770									

[a] From Wasson, 1974
[1] From Schaudy et al., 1972
[2] From Rasmussen et al., 1984
[3] From Campbell and Humayun, 2005
^ Gallegos, part of Ternera
# Listed as anomalous member of IVB group
* Detection limit

The origin of Willow Grove may be similar to that of Tishomingo. Both meteorites are structurally and chemically similar. Although both meteorites feature martensite structure, Tishomingo is characterized by plate martensite and Willow Grove is characterized by lath martensite. Lath martensite grows as parallel, elongate grains, while plate martensite grows in a blockier habit at irregular angles. This difference suggests a higher temperature of formation of martensite in Willow Grove, and therefore, a smaller temperature fluctuation between the original cooling of the meteorite and the martensite transformation (BIRCH et al., 2001).

Birch et al. (2001) speculated that outgassing at a high temperature could explain the volatile depletion observed in these two ungrouped irons. Furthermore, the high Ni and Co could be explained by coupling the outgassing with oxidation of chondritic material. Tishomingo and Willow Grove were conjectured to form when residual heat from impact melting of the parent-body promoted the slow growth of taenite. Once the taenite had formed, the material was modified.

TABLE 3: Tishomingo and Willow Grove Analyses from Birch *et al*., 2001

Meteorite	Cr µg/g	Fe wt%	Co wt%	Ni wt%	Cu µg/g	Ga µg/g	Ge µg/g	As µg/g	W µg/g	Re ng/g	Ir µg/g	Pt µg/g	Au µg/g
Willow Grove*	-	71	1.13	27.5	-	-	-	-	-	-	-	-	-
Willow Grove‡	170	-	1.21	27.9	10	0.23	<40	0.783	1.52	2550	17.4	23.7	0.233
Tishomingo‡	100	-	1.26	32.1	18	0.25	0.088	0.5	0.2	1640	17.4	-	0.144

* Electron microprobe
‡ Neutron activation

3. Samples

This study investigates eleven of the twelve members of the IVB group of iron meteorites and an additional three ungrouped meteorites. Most studies of IVB irons have not examined all members of the group. However, the published IVB data sets provide a

good background of the characteristics of the group IVB meteorites that can be expanded and used as a diagnostic tool to explore potential relationships between ungrouped irons and members of the IVB group (Table 2). In general, the ungrouped irons have less literature than the grouped irons, and specifically, Chinga, Tishomingo and Willow Grove have had very little follow-up work beyond their initial publications (BIRCH et al., 2001; IVES et al., 1978; RASMUSSEN et al., 1984; SCHAUDY et al., 1972; WASSON, 1974).

Table 4: Summary of Microstructure and Mineralogy of IVB and Ungrouped Irons

Name	Cape of Good Hope	Hoba	Iquique	Kokomo	Santa Clara	Skookum
Weight	136 kg	60,000 kg	12.5 kg	1.8 kg	63 kg	16 kg
Country of origin	South Africa	Grootfontein, Namibia	Tarapaca Chile	Indiana, USA	Durango, Mexico	Yukon Territory, Canada
Date	1793	1920	1871	1862	1976	1905
Troilite	√	√	√	absent	√	√
daubreelite	√	√	√	√		
schriebersite	√ streaks of α and β taenite	√ intergrowth of α and β taenite, oriented sheen	√ matte sheen	√ macroscopic parallel bands, scattered kamacite	√	√ matte structure

Name	Tawallah Valley	Ternera	Tlacotepec	Warburton Range	Weaver Mountains	Tinnie
Weight	75.75 kg	1.98 kg	71 kg	56.93 kg	38.8 kg	15.3 kg
Country of origin	northern Australia	Atacama, Chile	Puebla, Mexico	Western Australia	Arizona, USA	New Mexico, USA
Date	1939	1891	1903	1963	1898	1978
Troilite	√		√	√	√	
daubreelite	absent		√		√	
schriebersite	√ Kamacite forms as spindles	absent No parallel banding, kamacite and taenite form a sponge-like matrix	√ dark and light bands, kamacite spindles	√ Mottled ataxite structure, Silicate inclusions remain unconfirmed	√ oriented sheen, tiny silicate or glass shards	

Name	Chinga	Tishomingo	Willow Grove
Weight	209.4 kg	260 kg	11.7 kg
Country of origin	Respublika Tyva, Russia	Oklahoma, USA	Victoria, Australia
Date	1913	1965	1995
Troilite	√	√	
daubreelite	√	√	
schriebersite	√	absent	√
	Kamacite spindles, schlieren bands Tridymite reported	coarse martensitic microstructure diffusionless transformation of taenite into martensite	coarse martensitic microstructure diffusionless transformation of taenite into martensite

4. Methods

4.1 Isotope Dilution Procedure

The methods used for the highly siderophile element analyses are based upon those of Shirey and Walker (1995), Cohen and Waters (1996) and Smoliar *et al.* (1996). A diamond edge wafering blade was used for cutting the metal. Sample weights (Table 5) were less than 0.100 grams for IVB irons, but slightly higher for the ungrouped irons.

To ensure against cross-contamination of samples, each sample had a dedicated water trough for cooling, and the wafering blade was cleaned between each sample by cutting a piece of carborundum. Once cut to the desired weight, each sample was polished, again using individual pieces of carborundum, to remove any oxidation residue. The cut and polished pieces were weighed and placed into quartz carius tubes for digestion.

The carius tube digestion follows the procedure described by Shirey and Walker (1995). Each carius tube was loaded with the appropriate amount of ^{190}Os and ^{185}Re spike so as to achieve a ^{190}Os/^{192}Os ratio of approximately 1.2. A mixed spike of ^{105}Pd,

^{194}Pt, ^{99}Ru and ^{191}Ir was also added to achieve a $^{194}Pt/^{195}Pt$ ratio of approximately 2.1. Aqua regia was added to the carius tube, which was then sealed with a hydrogen torch. Sealed tubes were encased in a metal sleeve and placed in an oven at 240°C for at least 48 hours to allow for complete dissolution of sample (SHIREY and WALKER, 1995).

Once cooled, the carius tubes were removed from the oven and opened. The contents were frozen to prevent loss of sample and an aliquot of approximately 10% of each sample was set aside for bulk siderophile and chalcophile element analysis. Using the method described by Cohen and Waters (1996) osmium was extracted from the remaining solution using carbon tetrachloride (CCl_4) and the aqua regia, sans Os, was set aside for later siderophile element separation. The Os was back extracted from the CCl_4 into concentrated HBr. The HBr was dried and the remaining Os was microdistilled to further purify the sample (COHEN and WATERS, 1996). The separation of the remaining highly siderophile elements was accomplished through the use of Eichrom AG1X8 anion exchange resin. Elutions of 4M nitric acid (HNO_3), concentrated HNO_3, and 9M hydrochloric acid (HCl) remove Re, Ru, Pt and Ir, and Pd, respectively. Osmium purified by microdistillation, and the separate HSE cuts were then ready for analysis by mass spectrometry.

4.2 Mass Spectrometry

This study used two mass spectrometers for the purposes of sample analysis: inductively-coupled plasma mass spectrometry (ICP-MS) and thermal ionization mass spectrometry (TIMS). The HSE column cuts of the highly siderophile elements (Re, Ru, Ir, Pt and Pd) were analyzed by ICP-MS (Nu Plasma) while the microdistilled Os samples were analyzed by TIMS.

Before Nu Plasma analysis, each sample was diluted in 2% Nitric acid to a suitable concentration for signal stability. In most cases, a second dilution was necessary due to the high concentration of the HSE in the aliquots. Each HSE was analyzed separately using faraday cups and in increasing order of added spike to minimize background effects. The analysis of the HSE required the machine to be calibrated for each element. Standard solutions were interspersed throughout the analysis session to monitor magnet drift and to assist in the calculation of the error associated with the given analysis. Data from these standard solutions was also used to determine a fractionation factor that was used to correct the raw sample data. Concentrations of the standard solutions used are given in Appendix A.

For TIMS analysis, the samples were loaded on a platinum filament and heated to achieve a sufficient signal of at least 1 volt before analysis commenced. In some cases, a Daly detector was used in to find the signal. The analysis of osmium blanks were dispersed between the samples throughout the analysis session.

4.3 Error Analysis

It is important to determine the errors associated with the mass spectrometric analyses in order to accurately describe the precision of the data set. Errors can occur at many stages in the sample digestion process as well as during the collection of data by mass spectrometry. The first error encountered is during sample preparation and is associated with the weight of sample and spike. Assessment of this error is accomplished by comparing the weight of a known object made at different times and dates to evaluate the accuracy of the balance used and the reproducibility of the operator. In the case of this study, two different balances were used, one to measure the weight of the sample

added to the carius tube, another to measure the weight of spike added. The magnitude of this error was an average 0.017%. This was calculated using the standard deviation of replicate weights for an object as described in Appendix A, Table A1.

A second source of error comes from the spectrometry instruments. This can be observed through repeat measurements of a sample, as well as the reproducibility of standard solutions (Table A2). The latter reason is accounted for by dispersing standard solutions of known concentration throughout the analyses of samples with a minimum of three standard measurements per analytical session, namely at the beginning, middle and end of each set of samples.

5. Results and Interpretation

5.1 Highly Siderophile Element Systematics

Chondrite normalized HSE patterns for the IVB are highlighted by nested patterns. The elements are plotted in order of increasing volatility (Figure 4). Concentration of Re, Os, Ru and Ir is inversely related to weight percent Ni in the irons. Samples with higher Re, Os, Ru and Ir correspond to lower Ni contents, while sample having higher Ni contents have a lower concentration of these same HSE. Platinum plots within a very limited range of concentration (31.14 to 32.67 ppm), a value significantly enriched from chondritic Pt concentrations [~.859; (ANDERS and GREVESSE, 1989)]. Palladium is the only incompatible HSE shown in the pattern of IVB irons.

Table 5: IVB and Ungrouped Iron Osmium Isotope and HSE Data

	Weight	$^{187}Re/^{188}Os$	$^{187}Os/^{188}Os$	2SDM %	Re	Os	Ir	Ru	Pt	Pd
Cape of Good Hope Set 1	0.05944	0.3235	0.12092	0.017	3249.5	48355	30848	30703	30026	5378.4
Cape of Good Hope Set 4	0.08037	0.3222	0.12102	0.020	3224.3	48175	31914	30387	31189	5233.7
Hoba Set 1	0.06861	0.3355	0.12188	0.014	2731.5	39197	26863	29436	30142	6244.1
Hoba Set 4	0.05343	0.3349	0.12188	0.04	2729.8	39249	28278	28860	31422	6151.9
Iquique Set 4	0.06315	0.3242	0.12100	0.02	3243.1	48156	32189	30608	31147	5287.0
Kokomo* Set 4	0.08156	0.3235	0.12101	0.018	3144.1	46780	31372	30094	31186	5514.4
Santa Clara Set 4	0.08853	0.3703	0.12470	0.02	1808.8	23528	19792	25655	32317	8055.6
Skookum Set 2	0.07273	0.3900	0.12620	0.02	1356.2	16751	15814	23924	30826	9428.2
Skookum Set 4	0.04958	0.3895	0.12620	0.04	1450.6	17939	16815	24048	32501	9412.2
Tawallah Valley Set 1	0.06547	0.3954	0.12656	0.026	1377.6	16783	15178	23817	31242	9750.8
Tawallah Valley Set 4	0.05318	0.3940	0.12656	0.044	1372.6	16784	15578	23568	32674	9690.8
Ternera* Set 4	0.07418	0.3771	0.12525	0.068	1509.7	19283	17280	23926	32429	9567.0
Tlacotepec Set 1	0.07721	0.3240	0.12095	0.011	3155.2	46876	30169	30459	30132	5691.6
Tlacotepec Set 2	0.06772	0.3233	0.12096	0.015	3139.3	46742	29935	29998	29688	5679.2
Tlacotepec Set 4	0.06045	0.3232	0.12096	0.02	3135.7	46699	32108	30101	31259	5624.5
Warburton Range Set 1	0.09706	0.3980	0.12701	0.025	1290.9	15626	14427	23448	31365	10252
Warburton Range Set 4	0.07903	0.3976	0.12682	0.024	1284.2	15561	14805	23180	32750	10027.7
Weaver Mountain Set 1	0.08450	0.3887	0.12607	0.012	1468.5	18198	16105	24894	31328	8974.1
Weaver Mountain Set 4	0.07812	0.3869	0.12609	0.02	1475.6	18370	16940	24207	32618	8837.0
Willow Grove Set 4	0.05019	0.4375	0.12816	0.056	2878.6	31705	22252	24453	29974	10568.6
Chinga Set 2	0.09393	0.5646	0.14000	0.28	954.21	8156.5	4041.2	7679.0	9220.5	7063.2
Chinga Set 4	0.05915	0.5654	0.14015	0.019	991.38	8461.6	4132.6	7626.9	9587.7	6826.2
Tishomingo Set 2	0.09279	0.3316	0.12171	0.001	1690.4	24540	19867	25931	31492	8736.3
Tishomingo Set 4	0.07147	0.3333	0.12173	0.024	1704.6	24624	20631	25942	33159	8608.5

Set numbers refer which of four different chemical digestions the data was from. Set 1 analyzed six IVB irons. Set 2 analyzed 4 IVB irons, Chinga and Tishomingo, however due to human error in spiking and separation chemistry, only 4 samples yielded usable data. Set 3 was marred by human error in spiking and separation chemistry for all samples and yielded no usable data. Set 4 analyzed all samples of interest to this study yielding usable data for each sample. The data plotted in figures 4 – 9 all came from Set 4.

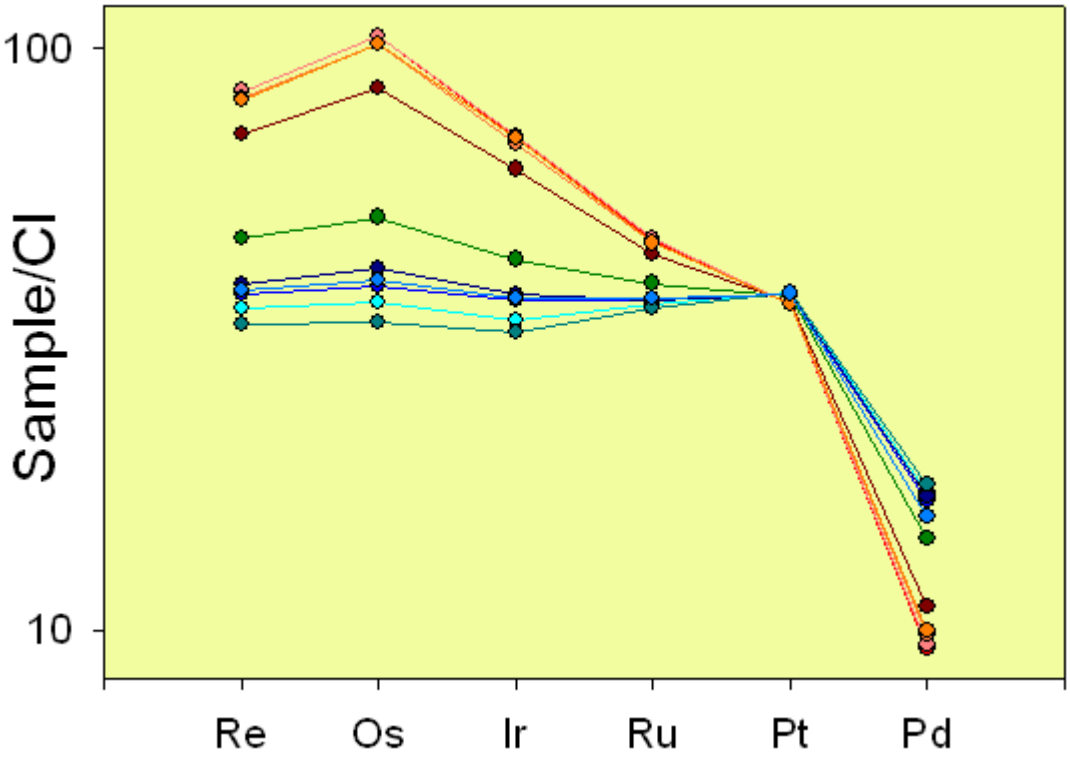

Figure 3: Diagram of highly siderophile elements versus concentration in each sample normalized to CI chondrites (ANDERS and GREVESSE, 1989). Each line represents a different IVB iron, red samples are low nickel, earlier formed meteorites, blue samples are high nickel, more evolved meteorites. Weight percent nickel increases from the top to bottom of the graph. Circles represent actual data, lines connect data points to illustrate the pattern of concentration for the IVB group.

The lower nickel samples are presumed to have formed first because Ni behaves incompatibly and prefers to remain in the melt. Palladium behaves incompatibly as well, showing an increasing concentration in the later-formed, higher Ni solids. By contrast, Re, Os, Ir and Ru are compatible, and prefer the solid state, where their initial concentration will be higher than in later forming solids. The apparent split of the IVB group between low and high Ni was termed the "compositional hiatus" by Rasmussen et al. (1984) and could be submitted as evidence for two parental regions of IVB irons. However, it is more likely attributable to incomplete sampling of the IVB parent body; by the calculations of Rasmussen et al.(1984), approximately 26% of the IVB parent body has not been sampled.

The IVB pattern is distinctive from other groups by pattern shape, limited range in Pt concentration, Ni correlation, and Pd incompatibility. Therefore, in order to be considered as having a possible relationship to the IVB group, ungrouped irons would need to have an HSE pattern very similar to the nested pattern observed for the grouped irons (Figure 3). The ungrouped irons, when plotted with the group IVB iron data, show varying levels of agreement with the IVB group (Figure 4).

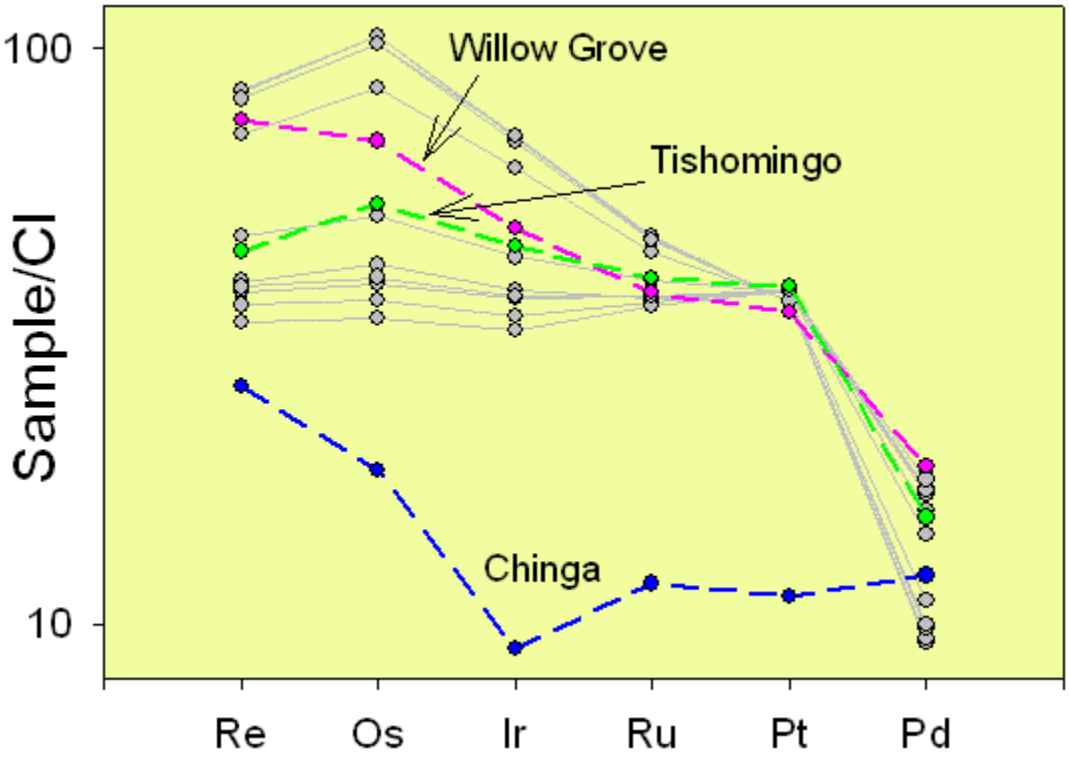

Figure 4: Graph of highly siderophile elements versus concentration in sample normalized to CI chondrites (ANDERS and GREVESSE, 1989). IVB irons are represented by grey lines, ungrouped irons of interest by dashed colored lines. Circles represent actual data points.

Chinga [Ni = 16.5 wt%; (RASMUSSEN et al., 1984)] has a different HSE pattern than that of the group IVB irons. The HSE pattern of Willow Grove [Ni = 27.9 wt%; (BIRCH et al., 2001)] is comparable to that of the group IVB irons, although there are some slight differences. The concentration of platinum falls slightly below the range of platinum for the IVB irons (29.97 ppm as compared to 31.14 ppm; Table 5). Also, the Re concentration relative to Os is higher, which is not the case for the IVB irons.

The HSE pattern of Tishomingo [Ni = 32.1 wt%; (BIRCH et al., 2001)] closely mirrors the nested pattern of the IVB irons, Santa Clara [Ni = 17.19 wt%; (RASMUSSEN et

al., 1984)] in particular. Based on the HSE pattern presented here, Tishomingo is the best possible match to the group IVB irons of the three ungrouped irons analyzed in this study, however a good argument in support of Willow Grove as a match to the IVB group could also be made.

5.2 Re-Os Systematics

The $^{187}Re/^{187}Os$ system is used to determine the ages of the iron meteorites in this study. In this system, ^{187}Re decays to ^{187}Os by beta decay with a half-life of 41.6 Ga. This long half-life makes Re-Os the ideal system to apply to iron meteorites, which would be expected to have a crystallization age near 4.56 Ga. Both Re and Os are considered highly siderophile and chalcophile and are found concentrated in planetary cores, including iron meteorite samples. Re and Os are compatible elements that prefer solid-metal to liquid-metal, and as a result of solid metal – liquid metal partitioning, the concentration of Re and Os will decrease in the residual melt as core crystallization proceeds.

TABLE 6: Re-Os Data for IVB irons from previously published studies

Sample	Re	Os	$^{187}Re/^{188}Os$	error	$^{187}Os/^{188}Os$	error
Tlacotepec^	3213	4792	0.3226	0.0002	0.12089	0.00002
Hoba^	2847	4090	0.335	0.0004	0.12189	0.00002
Replicate^	2858	4101	0.3354	0.0003	0.12192	0.00001
Tawallah Valley^	1407	1718	0.3944	0.0005	0.12657	0.00004
Warburton Range*	1303.1	15702	0.3998	0.0006	0.126896	0.00001
Tawallah Valley*	1386.6	16894	0.3954	0.0006	0.12658	0.000022
Weaver Mountain*	1493.4	18497	0.3889	0.0006	0.126097	0.000059
Replicate*	1493.3	18469	0.3895	0.0006	0.126097	0.000014
Hoba*	2757.3	39391	0.337	0.0005	0.121947	0.000033
Tlacotepec*	3165.9	47007	0.3242	0.0005	0.120944	0.000052
Replicate*	3168.2	47030	0.3243	0.0005	0.121027	0.000023
Cape of Good Hope*	3271.7	48743	0.3231	0.0005	0.120945	0.000056
Replicate*	3270.4	48623	0.3238	0.0005	0.120949	0.000021

Re and Os concentrations in ppb. Ratio errors are 2σ
^ From Shen et al., 1996
* From Smoliar et al., 1996

Previously published Re-Os isotope systematics for the IVB irons have shown that the IVB irons have a limited variation in $^{187}Re/^{188}Os$, which defines a less precise isochron than groups with a large range (SMOLIAR et al., 1996). Shen et al. (1996) combined their $^{187}Re/^{188}Os$ results for the IVA and IVB irons. By increasing the range of $^{187}Re/^{188}Os$, a more precisely defined isochron was obtained. Smoliar et al. (1996) also determined that the IVB isochron plots above the chondritic evolution path suggesting the $^{187}Os/^{188}Os$ ratio is higher than the bulk solar nebula assumption. The findings of Smoliar et al. (1996) imply that the IVB irons were derived from a melt with at least 10 times the concentration of chondritic melt, but with a sub-chondritic $^{187}Re/^{188}Os$ ratio.

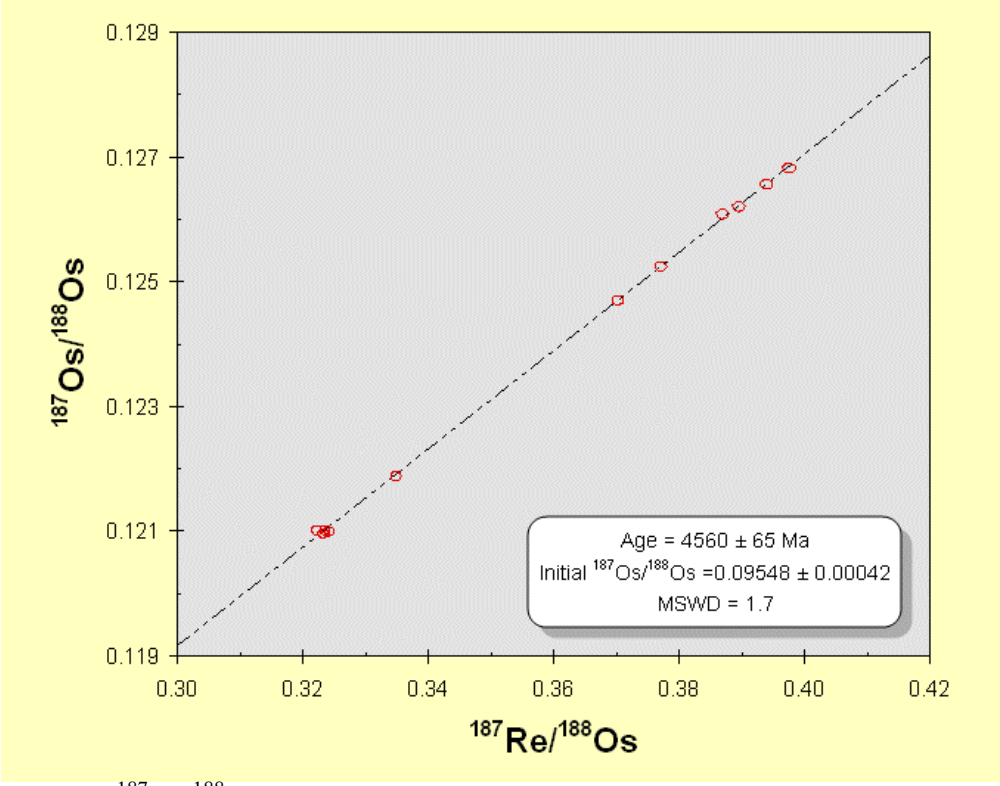

Figure 5: $^{187}Re/^{188}Os$ isotopic crystallization ages determined for the IVB irons.

The Re-Os isotope systematics have produced a crystallization age consistent with previously published data for a small group of IVB irons (SHEN et al., 1996; SMOLIAR et al., 1996). This study has determined a crystallization age of 4560 ± 65 Ma (MSWD = 1.7; Figure 5) and initial $^{187}Os/^{188}Os$ of 0.09548 ± 0.00042. Model ages calculated from the data of Shen et al. (1996) and Smoliar et al. (1996) for three and six IVB irons are 4570 ± 47 Ma (MSWD = 0.65) and 4528 ± 28 Ma (MSWD = 1.5), respectively, using Model-3 age determinations in Isoplot. These ages are consistent with early solar system crystallization.

Chinga and Willow Grove cannot be plotted on the same isochron as the IVB irons without drastic effect to the age and MSWD. Tishomingo can be plotted on the same isochron with minimal effect on the age or MSWD. In fact, the addition of Tishomingo to the IVB isochron marginally improves the precision of the age and has no effect on the MSWD (4566 ± 63 Ma, MSWD = 1.7). Furthermore, the initial $^{187}Os/^{188}Os$ (0.09543 ± 0.00040) does not show a significant change with the addition of Tishomingo.

5.3 Fractional Crystallization Modeling

Fractional crystallization has been used in previous studies to model the formation of the IVB irons (CAMPBELL and HUMAYUN, 2005; RASMUSSEN et al., 1984). However, these previous studies have used the distribution coefficient of Ni to determine the D values of other elements, and in this study, the D value of Ir was used to calculate the D values for the remaining highly siderophile elements. In this study, the fractional crystallization model uses as a starting point the experimentally determined $D_{0(Ir)}$ based on an assumed sulfur and phosphorous in the initial iron-bearing metal (CHABOT and

JONES, 2002). This method allows us to track the evolving concentrations of S and P in each increment of residual melt while simultaneously monitoring the HSE concentrations as the D value evolves. D values assumed for S and P are negligible, and the total relative change in D for these elements is very small. The evolution in D_{Ir} was calculated using the Chabot and Jones (2002) parameterization (2):

$$(2) \qquad \frac{1}{D_{Ir}} = \frac{\left[\frac{(1-2X_S-3X_P-3X_C)}{(1-X_S-2X_P-2X_C)}\right]^{\beta}}{D_{0(Ir)}}$$

where X_E is the molar fraction of the element in the system, β is a constant specific to the parameterized element (in this case, Ir), $D_{0(Ir)}$ is an experimentally determined D value for Ir, and D_{Ir} is the calculated partition coefficient from the parameterization. This calculated value of D_{Ir} is used to calculate the D values of Re, Os and other highly siderophile elements using the relationship described by Scott (1972) relating the slope of a log-log plot (Figure 6) to D values (3):

$$(3) \qquad Slope = \frac{(D_E - 1)}{(D_{Ir} - 1)}$$

where D_{Ir} is the distribution coefficient for iridium, and D_E is the distribution coefficient of another highly siderophile element. From this relationship and an assumed D_{Ir} from Chabot and Jones (2002), the remaining D values are established (Table 7 and B1).

Table 7: Log-log regressions from Figure 7

initial D_{Ir} = 1.5	Pt	Ru	Os	Re	Pd
Slope	-0.058	0.351	1.490	1.213	-0.813
Error	0.072	0.075	0.130	0.1	0.084
MSWD	0.22	0.094	0.160	0.18	0.25
D_o	0.97	1.18	1.75	1.61	0.59

The fractional crystallization model employed here to describe the formation of the IVB irons is the same model that has been applied to the ungrouped irons. If these ungrouped irons are from the same parent body, and if that parent body formed all solids

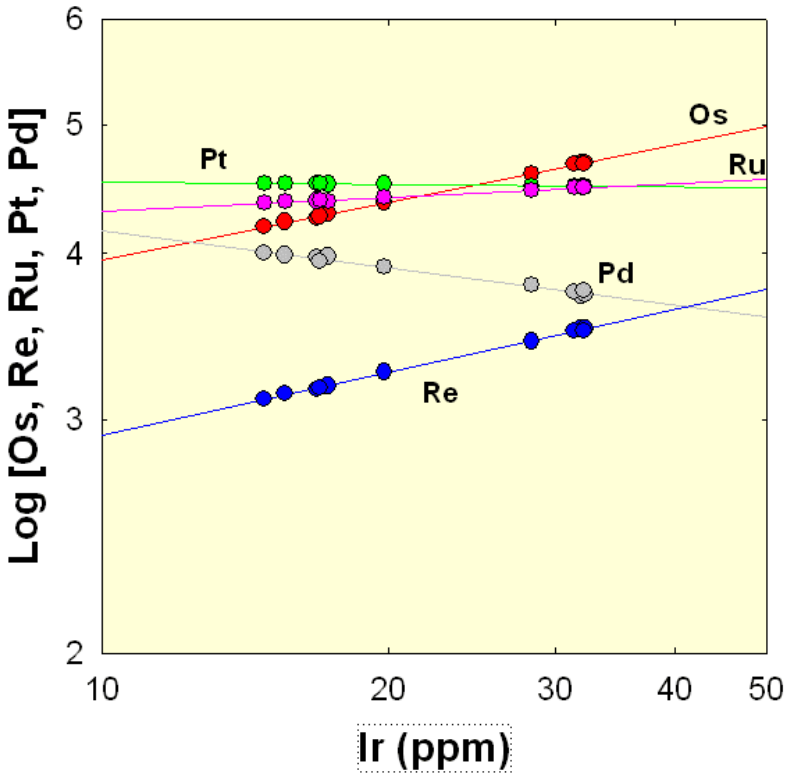

Figure 6: Log-Log diagram of the concentration of highly siderophile elements relative to concentration of Ir for the IVB irons only. Slope, error and MSWD of these trends are given in Table 7.

by fractional crystallization, then one model should accurately detail the process of formation. Using the same parameterization for D values used for the IVB irons, calculation by the equation of Scott (1972), does not account for D value variations in the formation of two of the ungrouped irons, Willow Grove and Chinga. Both of these irons

plot well off the relative trends of the HSE on the log-log diagram presented (Figure 7), and cannot be accurately modeled in this fractional crystallization calculation.

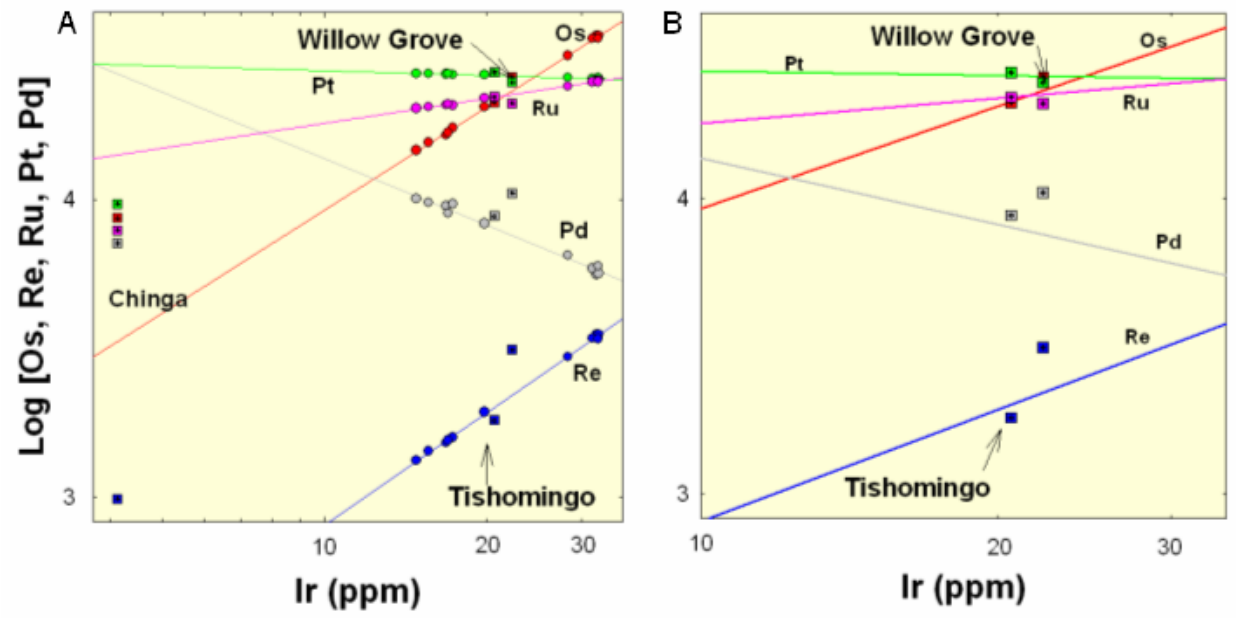

Figure 7: Log-Log diagram of concentration of the highly siderophile elements relative to Ir for the IVB irons (circles) and the ungrouped irons (squares). a) IVB irons and all ungrouped irons, b) trend of IVB irons and ungrouped irons Willow Grove and Tishomingo

The fractional crystallization model that was determined using the combined D value parameterization of Scott (1972) and Chabot and Jones (2003) provides a good description of the formation of the IVB irons (Figure 9). All IVB irons plot within the liquid and solid tracks, and represent a range from approximately 5 to 65 % fractionally crystallized. This is a smaller range of degree of crystallization than the previously determined range of 4 – 92 % (RASMUSSEN et al., 1984). However, this larger range was divided into high and low Ir groups, with 4 – 51 % and 77 – 92 % degree for crystallization for these subsets, respectively.

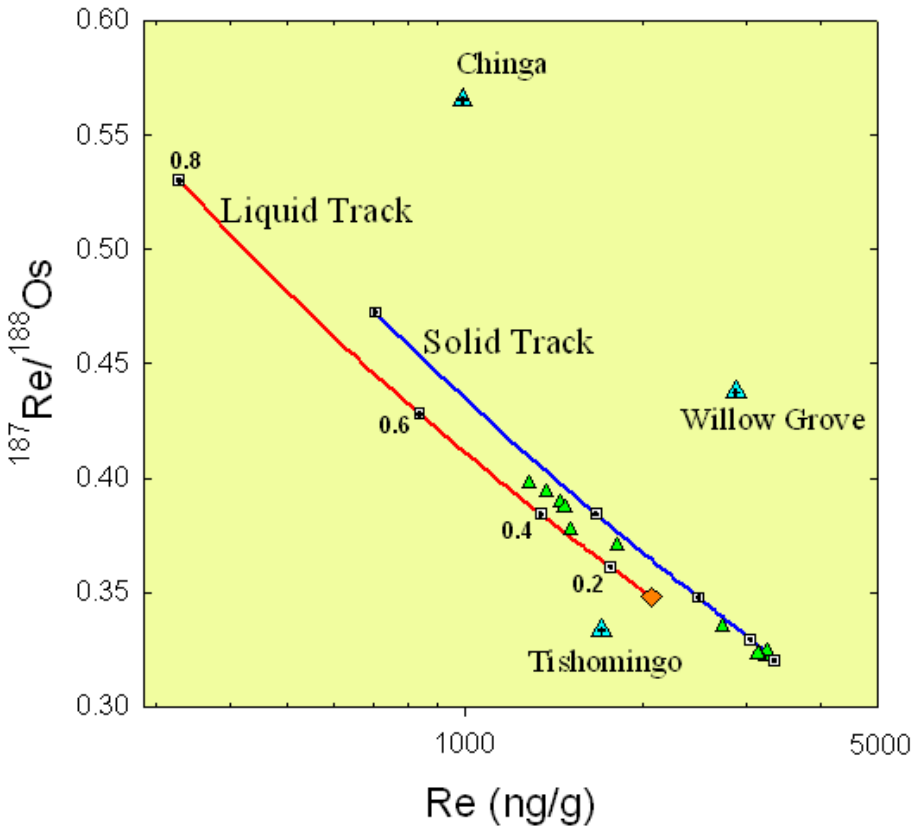

Figure 8: Fractional crystallization model of IVB irons. Green triangles represent IVB irons, Aqua triangles represent ungrouped irons, Red line is the solid track, blue line is the liquid track, and orange diamond is initial melt.

The resulting fractional crystallization model from the IVB irons with the ungrouped irons plotted in addition the IVB group is illustrated in figure 9. As determined by Smoliar et al. (1996), the IVB irons a derived from a non-chondritic parent-body with a sub-chondritic $^{187}Re/^{188}Os$ and a super-chondritic concentration of Re and Os. The initial concentration used in the fractional crystallization model was chosen to maximize Re/Os and minimize concentration of Re, so as to end up with an initial melt as close to chondritic values as possible for this non-chondritic system. The starting composition of this model (orange diamond) is Re_I = 2075 ppm and $^{187}Re/^{188}Os_I$ = 0.348.

As predicted from figure 8, neither Chinga nor Willow Grove can be modeled using the same calculation used for the IVB irons. Chinga, which plots with a lower Re concentration and a higher $^{187}Re/^{188}Os$, cannot be formed from the predicted starting composition of this model of IVB iron formation. By contrast, Willow Grove shows a significant enrichment in the concentration of Re in the sample while still within an acceptable range of $^{187}Re/^{188}Os$. Since Willow Grove plots well to the right of the solid track, this ungrouped iron, like Chinga, cannot be formed from the predicted initial composition of the IVB parent body.

Tishomingo, while plotting below the liquid track, can still be formed from the same fractional crystallization model used to describe the IVB irons. However, to use the IVB model of formation to explain the origin of Tishomingo, non-equilibrium mixing of an early formed solid (such as Cape of Good Hope) and a highly evolved liquid (greater than 70% fractionally crystallized) is necessary. Through this mixing process, a solid with a composition of Tishomingo would plot on the model determined for the IVB irons. There is however a problem with fitting Tishomingo to the IVB iron model; the anomalously high weight percent nickel of the ungrouped iron relative to the IVB irons.

Tishomingo has nearly twice the amount of nickel (32.1 wt %) than the members of the IVB group. It is not possible to model such a high concentration of Ni from the initial IVB parent body with simple fractional crystallization. If the IVB parent body were to have evolved to such a high Ni content as to form Tishomingo, there should be a similar enrichment in the HSE. However, as previously mentioned, the HSE pattern and Pt concentration of Tishomingo agrees with the pattern and concentration of the IVB irons.

If, similar to the suggestion for IVB Ni enrichment of Rasmussen et al. (1984), the high Ni of the Tishomingo parent-body is due to oxidation, then an increase in the concentration of highly siderophile elements relative to the IVB group should be observed. With respect to the limited range of platinum, there is no notable increase in concentration. Another hypothesis is that Tishomingo formed from a unique Ni-rich parent-body in a different part of the nebula, independent from and unrelated to the IVB parent-body. This poses a problem in that the likelihood of forming a body of nearly identical composition in a different part of the nebula is highly, although not entirely, improbable.

6. Summary and Conclusions

This study has taken eleven of the twelve members of the IVB iron meteorite group, constrained their crystallization age by the Re-Os isotopic system, determined their highly siderophile element composition using isotope dilution, and presented a fractional crystallization model for the formation of this small but unique group of irons. Two ungrouped irons and one anomalous iron were analyzed to explore possible relationships to the IVB group. These irons, Chinga, Tishomingo and Willow Grove, each had similarities to the composition of the IVB group. However, there are notable differences that set these irons apart from the IVB group.

The IVB irons have a crystallization age of 4575 ± 56 Ma is consistent with ages previously determined (SHEN et al., 1996; SMOLIAR et al., 1996). The highly siderophile element composition of the IVB irons have similar patterns of relative concentrations which co-vary with Ni content. IVB irons have a very limited range of concentration of

platinum, and platinum content can be used as a good indicator of members of the IVB group. The fractional crystallization model for the IVB irons describes the formation of the group starting from a non-chondritic parent-melt, and has determined that the IVB group is comprised of samples representing some of the earliest formed solids from this non-chondritic melt (Cape of Good Hope), as well as some later formed solids that were crystallized after > 50% fractional crystallization had occurred (Warburton Range).

Chinga, although originally classified as a IVB iron (BUCHWALD, 1975; SCHAUDY et al., 1972; WASSON, 1974), is unrelated to the IVB group due to differences in highly siderophile element pattern, concentration of platinum, and its inability to be modeled as having formed along the same fractional crystallization path as the IVB irons. Willow Grove, while showing many similarities with respect to highly siderophile element pattern and platinum concentration, poses a problem of formation using the fractional crystallization modeled here employed. In addition, it is impossible to plot Chinga and Willow Grove on an isochron for the IVB irons. Tishomingo could possibly be a IVB iron. Its highly siderophile element systematics are in agreement with those of the IVB group, and the platinum concentration falls within the limited range of the IVB group. Furthermore, the formation of Tishomingo can be explained by the same fractional crystallization model used to describe the IVB group, if Tishomingo was the result of non-equilibrium mixing of an early formed solid and a highly evolved liquid. Tishomingo can also be successfully plotted on the isochron of the IVB irons, agreeing with both the age and closed system behavior of the group. However, like Willow Grove, the high percent of nickel still needs to be explained in the context of IVB formation if Tishomingo is to be grouped with the IVB irons.

Appendix A: Samples, Methods and Errors

A.1 Sample Descriptions

Cape of Good Hope has a total mass of 136 kg and was found in South Africa in 1793. Some etched sections of this meteorite show diffuse streaks of α and β taenite phases thinning over a length of several centimeters (BUCHWALD, 1975). Accessory phases found in Cape of Good Hope include troilite visible with the naked eye and measuring up to 3 mm nodules, schriebersite substituted for taenite at a micron scale, and daubreelite, a chromium sulfide found as lamellae in troilite nodules.

Hoba is the largest meteorite found on Earth. Weighing over 60,000 kilograms, the main mass of Hoba has remained in Namibia at the farm where it was found in 1920. Etched sections of Hoba show no visible kamacite lamellae but do show an oriented sheen. Similar to Cape of Good Hope, under high magnification, an intergrowth of α and β taenite are observed (BUCHWALD, 1975). Schriebersite, troilite and daubreelite inclusions are found in the sample, in some cases acting as nuclei for kamacite growth.

Iquique was found in Chile in 1871 and weighed 12.5 kg. Etched sections of Iquique show a matte sheen, and parallel bands. Schreibersite and troilite both occur as inclusions, the latter being visible to the naked eye. Daubreelite occurs as lamellae in sulfide nodules. The microstructure of Iquique is similar to that of Hoba, Kokomo and Tlacotepec (BUCHWALD, 1975).

Kokomo was found in Indiana in 1862. A total of 1800 grams of the iron has been recovered. Similar to the previously described IVB irons, Kokomo also has macroscopic parallel banding visible in etched sections. Scattered kamacite occur in the matrix, as do schriebersite and daubreelite, while troilite is notably absent (BUCHWALD, 1975).

Santa Clara, with a total mass of 63 kg, was found in Durango, Mexico in 1976. Santa Clara is the midpoint of the IVB meteorites analyzed in that it contains the median concentration of nickel.

Skookum was found in Canada's Yukon Territory in 1905. The 16 kg mass was originally labeled as part of the meteorite Klondike, however, in 1989, the Meteoritical Society recognized the two masses of Klondike as two separate meteorites, Skookum and Gay Gulch. Skookum displays a matte structure and scattered troilite nodules in etched sections, with no other observable inclusions. Bands of taenite, similar to those observed in Hoba and Tlacotepec, are also observed, although they are slightly narrower in Skookum than in the other IVB irons. Schriebersite grains are often found with taenite halos. This iron has been reheated, making it not quite similar to the other IVB irons. However prior to reheating, it most likely resembled Tawallah Valley (BUCHWALD, 1975).

Tawallah Valley is a 1939 find from northern Australia. The total mass of Tawallah Valley is 75.75 kg. Etched sections show an oriented sheen with very few troilite inclusions. Kamacite forms as spindles and as blebs which appear to nucleate from small phosphides. Phosphides are evenly distributed throughout the iron and measure no larger than 15 microns. Scattered nodules of troilites up to 2 millimeters across are twinned. Tawallah Valley closely resembles the appearance of Warburton range, Weaver Mountains, and the aforementioned Skookum (BUCHWALD, 1975).

Ternera is an 1891 find from central Chile that yielded 1980 grams of meteorite. Etched sections show no parallel banding as was observed in other IVB irons. Kamacite and taenite form a sponge-like matrix on the microscopic scale. No phosphides have been found in Ternera. Structurally, Ternera is unique among the IVB group, however chemically it falls within the IVB range. It has been suggested that Ternera is possibly related to Galleguillos, which is postulated to be a reheated sample that was part of the Ternera shower (BUCHWALD, 1975).

Tlacotepec was found in Puebla, Mexico in 1903. The sample weighs 71 kg. Etched sections of Tlacotepec show dark and light bands, similar to those observed in other IVB irons and consistent with the structure of ataxites. Kamacite spindles are observed in clusters, they are both small (less than 30 microns wide) and infrequent, and nucleate from phosphides or sulfides. Schreibersite and troilite inclusions occur in Tlacotepec, although the former is much less frequent than the latter. Daubreelite lamellae are found within some troilite grains. Tlacotepec shows no evidence of carbides, silicates or graphite (BUCHWALD, 1975).

Warburton Range is a 1963 find from Western Australia weighing 56.93 kg. Mottled ataxite structure and scattered troilite inclusions are visible in etched sections. Troilite and schriebersite have both been observed in Warburton Range. Silicate inclusions have been reported, but remain unconfirmed in the meteorite. Warburton Range most closely resembles the structure of Skookum, Weaver Mountains and Tawallah Valley (BUCHWALD, 1975).

Weaver Mountains was an 1898 fall of 38.8 kg in central Arizona. An oriented sheen is visible in etched sections of Weaver Mountains. Schreibersite occurs as evenly distributed blebs throughout the sample. Troilite nodules up to 4 mm across have been observed throughout the metal mass. Daubreelite is also observed in the meteorite, as are what appear to be tiny silicate or glass shards. Weaver Mountains most closely resembles Tawallah Valley, with both showing a different matrix than that observed in Hoba and Kokomo (BUCHWALD, 1975).

Chinga is a 209.4 kg meteorite from southeastern Russia, near Mongolia. This meteorite has very few sulfide and no phosphide inclusions. Kamacite spindles are visible on a microscopic scale and etched sections show schlieren bands (BUCHWALD, 1975). Chinga has the longest paper trail of the ungrouped irons of interest in this study because it was initially classified as an anomalous member of the IVB iron group (BUCHWALD, 1975; SCHAUDY et al., 1972; WASSON, 1974). However, a more robust analysis of the IVB group by Rasmussen and colleagues (1984) would observe significantly lower Ir concentrations (3.6 and 3.9 ppm) of Ir for Chinga, as compared to the more enriched average of 21.2 ppm for the members of the IVB group reported (RASMUSSEN et al., 1984; SCHAUDY et al., 1972; WASSON, 1974).

Tishomingo, a 1965 find of 260 kg in Oklahoma, was originally stated to be unrelated to any other meteorite due to its unique, high Ni composition (BUCHWALD, 1975) and the distinctively coarse martensitic microstructure, which is indicative of diffusionless transformation of taenite into martensite (IVES et al., 1978). However, a more recent study (BIRCH et al., 2001) links Tishomingo to Willow Grove on the bases of both composition and microstructure, the seemingly unique features to only Tishomingo. Martensite transformation accounts for 80% of the volume and has an acicular habit.

Tishomingo contains no carbide, silicate or phosphide inclusions, it does however have scattered sulfide blebs of both daubreelite and troilite (BUCHWALD, 1975).

Willow Grove is an 11.7 kg, 1995 find from Victoria, Australia. The microstructure of this sample has also been transformed from taenite to martensite, similar to Tishomingo. Willow Grove also has a similar composition with respect to Ni and other indicative elements such as phosphorous (P), cobalt (Co), gallium (Ga) and gold (Au; Table 2). Tishomingo and Willow Grove fall within a range of other high Ni ungrouped irons, however, high Ni is the only similarity observed by Birch and colleagues. The other high Ni meteorites do not have the same martensitic structure nor the low P concentration that relates to Tishomingo and Willow Grove. Therefore, Tishomingo and Willow Grove were ruled out as having a possible genetic link to these other high Ni weight percent samples.

A.2 Standard Solutions

The concentrations of highly siderophile elements in the standard solutions used for ICP-MS analysis are 20 ppb Pt, 50 ppb Ir, 100 ppb Ru and Pd, and 200 ppb Re.

A.3 Error Analysis

The error associated with scale uncertainty when weighing samples is shown below (Table A1). The weights were averaged and a standard deviation (STD) calculated. From this STD, the error for each weighing was determined and converted to a percent error. The average percent error for each scale (Clean Lab and Plasma Lab) was then calculated to determine the total weighing error.

TABLE A1: Weighing Error Calculation

	Clean Lab	error	% error	Plasma Lab	error	% error
	0.42764	0.00008	0.018%	0.427688	0.00018	0.042%
	0.42766	0.00003	0.007%	0.427753	0.00003	0.006%
	0.42766	0.00003	0.007%	0.427740	0.00006	0.013%
	0.42765	0.00005	0.012%	0.427768	0.00001	0.002%
	0.42762	0.00012	0.029%	0.427768	0.00001	0.002%
	0.42767	0.00001	0.001%	0.427771	0.00002	0.004%
	0.42768	0.00002	0.004%	0.427804	0.00009	0.022%
	0.42780	0.00030	0.070%	0.427820	0.00013	0.031%
Average	**0.42767**		**0.018%**	**0.427764**		**0.015%**
STD	**5.5E-05**			**4.0E-05**		
		Weighing Error		**0.017%**		

The error calculation for the highly siderophile element isotopic ratios are shown below (Table A2). The absolute error (Abs. Error) is the error calculated by the mass spectrometer, while the error percent was calculated using the absolute error and the measured ratio. For the Os analysis, the error calculated by the mass spectrometer was given as a 2-sigma percent and the average error has been calculated.

TABLE A2: Error Calculation for HSE

	Abs. Error	Error (%)
$^{105}Pd/^{106}Pd$		
0.8213678	0.000521	0.063%
0.8216896	0.000441	0.054%
0.8062159	0.000042	0.005%
0.8098872	0.000206	0.025%
0.8096799	0.000164	0.020%
0.8033019	0.000021	0.003%
0.8133275	0.004580	0.563%
Average	***0.000854***	***0.105%***
$^{194}Pt/^{196}Pt$		
1.38682	0.000588	0.042%
1.277504718	0.000027	0.002%
1.27340845	0.000076	0.006%
1.277034904	0.000117	0.009%
1.275451958	0.000099	0.008%
1.275077699	0.000169	0.013%
Average	***0.000179***	***0.013%***
$^{186}Os/^{188}Os$		2σ (%)
0.1198639		0.004%
0.1198683		0.005%
0.1197582		1.014%
0.1198723		0.004%
0.1198511		0.006%
0.1198607		0.007%
0.1198587		0.003%
Average		***0.149%***
$^{187}Os/^{188}Os$		2σ (%)
0.1138879		0.008%
0.1138252		0.012%
0.1151291		0.956%
0.1138385		0.007%
0.1138052		0.020%
0.1138085		0.024%
0.1138128		0.008%
Average		***0.148%***

	Abs. Error	Error (%)
$^{185}Re/^{187}Re$		
0.5986091	0.000021	0.004%
0.5986008	0.000023	0.004%
0.5984435	0.000013	0.002%
0.5986262	0.000017	0.003%
0.5988782	0.000036	0.006%
0.5868378	0.000017	0.003%
0.5865672	0.000013	0.002%
0.6367647	0.000169	0.027%
0.6428294	0.000440	0.068%
0.5984836	0.000017	0.003%
0.5990299	0.000054	0.009%
0.5994278	0.000047	0.008%
Average	***0.000072***	***0.012%***
$^{191}Ir/^{193}Ir$		
0.5838818	0.000130	0.022%
0.5932673	0.000548	0.092%
0.59612	0.000716	0.120%
0.5830334	0.000014	0.002%
0.5836587	0.000023	0.004%
0.5841857	0.000020	0.003%
0.5577113	0.000152	0.027%
0.5838199	0.000022	0.004%
0.5850961	0.000077	0.013%
Average	***0.000189***	***0.032%***
$^{99}Ru/^{101}Ru$		
0.7483952	0.000051	0.007%
0.751333	0.000133	0.018%
0.7500595	0.000105	0.014%
0.7476958	0.000008	0.001%
0.7481209	0.000023	0.003%
0.7487501	0.000061	0.008%
0.7481002	0.000020	0.003%
0.7475999	0.000016	0.002%
0.7481373	0.000032	0.004%
0.7098359	0.000384	0.054%
Average	***0.000083***	***0.011%***

Appendix B: Fractional Crystallization Modeling Data

Simple fractional crystallization was used to model the formation of the IVB and ungrouped irons. While the model has been presented as figure 10 in the text, Table B1 shows the data from which the model was calculated and plotted. Using the calculated D values from Table 7, and an assumed starting composition (Re_I = 2075 ppm and $^{187}Re/^{188}Os_I$ = 0.348), determinations of the concentration or ratio value in the solid and liquid (C_S and C_L) were made for increasing degrees of fractional crystallization (*f-1*).

Table B1: D Value Determinations

mole fraction			Re	Os	Re/Os		mole fraction			Re	Os	Re/Os	
Xs	Xp	slope	1.213	1.49		F	Xs	Xp	slope	1.213	1.49		F
0.0001	0.0005		1.61	1.75	0.920	0	0.0206	0.0046		1.86	2.05	0.905	0.41
0.0006	0.0006		1.62	1.76	0.920	0.01	0.0211	0.0047		1.86	2.06	0.904	0.42
0.0011	0.0007		1.62	1.76	0.919	0.02	0.0216	0.0048		1.87	2.07	0.904	0.43
0.0016	0.0008		1.63	1.77	0.919	0.03	0.0221	0.0049		1.88	2.08	0.904	0.44
0.0021	0.0009		1.63	1.78	0.919	0.04	0.0226	0.005		1.88	2.09	0.903	0.45
0.0026	0.001		1.64	1.79	0.918	0.05	0.0231	0.0051		1.89	2.09	0.903	0.46
0.0031	0.0011		1.64	1.79	0.918	0.06	0.0236	0.0052		1.90	2.10	0.903	0.47
0.0036	0.0012		1.65	1.80	0.917	0.07	0.0241	0.0053		1.90	2.11	0.902	0.48
0.0041	0.0013		1.66	1.81	0.917	0.08	0.0246	0.0054		1.91	2.12	0.902	0.49
0.0046	0.0014		1.66	1.81	0.917	0.09	0.0251	0.0055		1.92	2.13	0.901	0.5
0.0051	0.0015		1.67	1.82	0.916	0.1	0.0256	0.0056		1.93	2.14	0.901	0.51
0.0056	0.0016		1.67	1.83	0.916	0.11	0.0261	0.0057		1.93	2.14	0.901	0.52
0.0061	0.0017		1.68	1.83	0.916	0.12	0.0266	0.0058		1.94	2.15	0.900	0.53
0.0066	0.0018		1.68	1.84	0.915	0.13	0.0271	0.0059		1.95	2.16	0.900	0.54
0.0071	0.0019		1.69	1.85	0.915	0.14	0.0276	0.006		1.95	2.17	0.900	0.55
0.0076	0.002		1.70	1.85	0.914	0.15	0.0281	0.0061		1.96	2.18	0.899	0.56
0.0081	0.0021		1.70	1.86	0.914	0.16	0.0286	0.0062		1.97	2.19	0.899	0.57
0.0086	0.0022		1.71	1.87	0.914	0.17	0.0291	0.0063		1.98	2.20	0.899	0.58
0.0091	0.0023		1.71	1.88	0.913	0.18	0.0296	0.0064		1.98	2.21	0.898	0.59
0.0096	0.0024		1.72	1.88	0.913	0.19	0.0301	0.0065		1.99	2.22	0.898	0.6
0.0101	0.0025		1.72	1.89	0.912	0.2	0.0306	0.0066		2.00	2.22	0.898	0.61
0.0106	0.0026		1.73	1.90	0.912	0.21	0.0311	0.0067		2.00	2.23	0.897	0.62
0.0111	0.0027		1.74	1.91	0.912	0.22	0.0316	0.0068		2.01	2.24	0.897	0.63
0.0116	0.0028		1.74	1.91	0.911	0.23	0.0321	0.0069		2.02	2.25	0.897	0.64
0.0121	0.0029		1.75	1.92	0.911	0.24	0.0326	0.007		2.03	2.26	0.896	0.65
0.0126	0.003		1.76	1.93	0.911	0.25	0.0331	0.0071		2.03	2.27	0.896	0.66
0.0131	0.0031		1.76	1.94	0.910	0.26	0.0336	0.0072		2.04	2.28	0.896	0.67
0.0136	0.0032		1.77	1.94	0.910	0.27	0.0341	0.0073		2.05	2.29	0.895	0.68
0.0141	0.0033		1.77	1.95	0.909	0.28	0.0346	0.0074		2.06	2.30	0.895	0.69
0.0146	0.0034		1.78	1.96	0.909	0.29	0.0351	0.0075		2.07	2.31	0.895	0.7
0.0151	0.0035		1.79	1.97	0.909	0.3	0.0356	0.0076		2.07	2.32	0.894	0.71
0.0156	0.0036		1.79	1.97	0.908	0.31	0.0361	0.0077		2.08	2.33	0.894	0.72
0.0161	0.0037		1.80	1.98	0.908	0.32	0.0366	0.0078		2.09	2.34	0.894	0.73
0.0166	0.0038		1.80	1.99	0.908	0.33	0.0371	0.0079		2.10	2.35	0.893	0.74
0.0171	0.0039		1.81	2.00	0.907	0.34	0.0376	0.008		2.10	2.36	0.893	0.75
0.0176	0.004		1.82	2.00	0.907	0.35	0.0381	0.0081		2.11	2.37	0.893	0.76
0.0181	0.0041		1.82	2.01	0.906	0.36	0.0386	0.0082		2.12	2.38	0.892	0.77
0.0186	0.0042		1.83	2.02	0.906	0.37	0.0391	0.0083		2.13	2.39	0.892	0.78
0.0191	0.0043		1.84	2.03	0.906	0.38	0.0396	0.0084		2.14	2.40	0.892	0.79
0.0196	0.0044		1.84	2.04	0.905	0.39	0.0401	0.0085		2.15	2.41	0.891	0.8
0.0201	0.0045		1.85	2.04	0.905	0.4							

Table B2: Fractional Crystallization Data Table

F	Re Cl	Re Cs	$^{187}Re/^{188}Os$ Cl	$^{187}Re/^{188}Os$ Cs	F	Re Cl	Re Cs	$^{187}Re/^{188}Os$ Cl	$^{187}Re/^{188}Os$ Cs
0	2075	3345	0.3481	0.3203	0.41	1320	2452	0.3860	0.3492
0.01	2062	3335	0.3486	0.3207	0.42	1296	2416	0.3876	0.3505
0.02	2049	3325	0.3491	0.3210	0.43	1272	2379	0.3893	0.3519
0.03	2036	3314	0.3496	0.3213	0.44	1248	2342	0.3910	0.3533
0.04	2022	3303	0.3502	0.3217	0.45	1223	2305	0.3928	0.3548
0.05	2008	3291	0.3507	0.3221	0.46	1199	2266	0.3946	0.3563
0.06	1994	3279	0.3513	0.3224	0.47	1174	2227	0.3965	0.3578
0.07	1979	3266	0.3519	0.3228	0.48	1149	2187	0.3984	0.3595
0.08	1965	3253	0.3525	0.3233	0.49	1123	2147	0.4005	0.3612
0.09	1950	3239	0.3531	0.3237	0.5	1098	2106	0.4026	0.3629
0.1	1934	3224	0.3537	0.3241	0.51	1073	2065	0.4047	0.3647
0.11	1919	3209	0.3544	0.3246	0.52	1047	2023	0.4070	0.3666
0.12	1903	3193	0.3551	0.3251	0.53	1021	1980	0.4093	0.3685
0.13	1886	3177	0.3558	0.3256	0.54	995.2	1937	0.4117	0.3706
0.14	1870	3160	0.3565	0.3261	0.55	969.2	1893	0.4142	0.3727
0.15	1853	3142	0.3572	0.3266	0.56	943.0	1849	0.4168	0.3749
0.16	1836	3124	0.3580	0.3272	0.57	916.9	1804	0.4195	0.3771
0.17	1819	3105	0.3588	0.3277	0.58	890.6	1759	0.4223	0.3795
0.18	1801	3086	0.3596	0.3283	0.59	864.3	1713	0.4252	0.3820
0.19	1783	3066	0.3604	0.3290	0.6	837.9	1667	0.4282	0.3845
0.2	1765	3045	0.3612	0.3296	0.61	811.5	1621	0.4314	0.3872
0.21	1747	3023	0.3621	0.3302	0.62	785.1	1574	0.4346	0.3900
0.22	1728	3001	0.3630	0.3309	0.63	758.7	1526	0.4380	0.3929
0.23	1709	2978	0.3639	0.3316	0.64	732.4	1479	0.4416	0.3959
0.24	1689	2955	0.3648	0.3323	0.65	706.0	1431	0.4453	0.3991
0.25	1670	2931	0.3658	0.3331	0.66	679.7	1383	0.4492	0.4024
0.26	1650	2906	0.3668	0.3339	0.67	653.5	1335	0.4532	0.4059
0.27	1630	2880	0.3679	0.3347	0.68	627.4	1286	0.4575	0.4096
0.28	1609	2854	0.3689	0.3355	0.69	601.4	1237	0.4619	0.4134
0.29	1589	2827	0.3700	0.3364	0.7	575.5	1189	0.4666	0.4174
0.3	1568	2800	0.3711	0.3372	0.71	549.8	1140	0.4715	0.4216
0.31	1546	2772	0.3723	0.3382	0.72	524.2	1091	0.4766	0.4261
0.32	1525	2743	0.3735	0.3391	0.73	498.8	1042	0.4821	0.4308
0.33	1503	2713	0.3747	0.3401	0.74	473.6	993.1	0.4878	0.4357
0.34	1481	2683	0.3760	0.3411	0.75	448.7	944.4	0.4938	0.4410
0.35	1459	2652	0.3773	0.3421	0.76	424.1	895.9	0.5003	0.4466
0.36	1436	2620	0.3786	0.3432	0.77	399.7	847.6	0.5071	0.4525
0.37	1414	2588	0.3800	0.3443	0.78	375.6	799.6	0.5143	0.4588
0.38	1391	2555	0.3814	0.3455	0.79	351.9	752.0	0.5220	0.4655
0.39	1367	2521	0.3829	0.3467	0.8	328.6	704.8	0.5303	0.4727
0.4	1344	2487	0.3844	0.3479					

Works Cited

Anders E. and Grevesse N. (1989) Abundances of the Elements - Meteoritic and Solar. *Geochimica Et Cosmochimica Acta* **53**(1), 197-214.

Birch W. D., Samuels L. E., and Wasson J. T. (2001) Willow Grove: A unique nickel-rich ataxite from Victoria, Australia. *Meteoritics & Planetary Science* **36**(9), A247-A254.

Bird J. M. and Weathers M. S. (1979) Origin of Josephinite. *Geochemical Journal* **13**(2), 41-55.

Buchwald V. F. (1975) *Handbook of Iron Meteorites*. University of California Press.

Campbell A. J. and Humayun M. (2005) Compositions of group IVB iron meteorites and their parent melt. *Geochimica Et Cosmochimica Acta* **69**(19), 4733-4744.

Chabot N. L. and Jones J. H. (2002) Parameterizing iron meteorite partitioning experiments. *Meteoritics & Planetary Science* **37**(7), A30-A30.

Cohen A. S. and Waters F. J. (1996) Separation of osmium from geological materials by solvent extraction for analysis by thermal ionisation mass spectrometry. *Analytica Chimica Acta* **332**(2-3), 269-275.

Cook D. L., Walker R. J., Horan M. F., Wasson J. T., and Morgan J. W. (2004) Pt-Re-Os systematics of group IIAB and IIIAB iron meteorites. *Geochimica Et Cosmochimica Acta* **68**(6), 1413-1431.

Goldstein J. I. and Short J. M. (1967) Iron Meteorites Their Thermal History and Parent Bodies. *Geochimica Et Cosmochimica Acta* **31**(10), 1733-&.

Haack H., Scott E. R. D., Love S. G., Brearley A. J., and McCoy T. J. (1996) Thermal histories of IVA stony-iron and iron meteorites: Evidence for asteroid fragmentation and reaccretion. *Geochimica Et Cosmochimica Acta* **60**(16), 3103-3113.

Ives L. K., Kasen M. B., Schramm R. E., Ruff A. W., and Reed R. P. (1978) Microstructural Study of Tishomingo Meteorite. *Geochimica Et Cosmochimica Acta* **42**(7), 1051-1066.

Lovering J. F., Nichiporuk W., Chodos A., and Brown H. (1957) The Distribution of Gallium, Germanium, Cobalt, Chromium, and Copper in Iron and Stony-Iron Meteorites in Relation to Nickel Content and Structure. *Geochimica Et Cosmochimica Acta* **11**(4), 263-278.

McDonough W. F. (2003) Compositional Model for the Earth's Core. In *The Mantle and Core*, Vol. 2 (ed. R. W. Carlson), pp. 547-568. Elsevier-Pergamon.

Mittlefehldt D. W., McCoy T. J., Goodrich C. A., and Kracher A. (1998) Non-chondritic Meteorites from Asteroidal Bodies. In *Planetary Materials*, Vol. 36 (ed. J. J. Papike), pp. 4-1 - 4-195. Mineralogical Society of America.

Rasmussen K. L., Malvin D. J., Buchwald V. F., and Wasson J. T. (1984) Compositional Trends and Cooling Rates of Group-IVB Iron-Meteorites. *Geochimica Et Cosmochimica Acta* **48**(4), 805-813.

Schaudy R., Wasson J. T., and Buchwald V. F. (1972) Chemical Classification of Iron-Meteorites .6. Reinvestigation of Irons with Ge Concentrations Lower Than 1 ppm. *Icarus* **17**(1), 174-&.

Scott E. R. D. (1972) Chemical Fractionation in Iron-Meteorites and Its Interpretation. *Geochimica Et Cosmochimica Acta* **36**(11), 1205-&.

Scott E. R. D., Haack H., and McCoy T. J. (1996) Core crystallization and silicate-metal mixing in the parent body of the IVA iron and stony-iron meteorites. *Geochimica Et Cosmochimica Acta* **60**(9), 1615-1631.

Sears D. W. (1978) Condensation and Composition of Iron-Meteorites. *Earth and Planetary Science Letters* **41**(2), 128-138.

Shen J. J., Papanastassiou D. A., and Wasserburg G. J. (1996) Precise Re-Os determinations and systematics in iron meteorites. *Geochimica Et Cosmochimica Acta* **60**(15), 2887-2900.

Shirey S. B. and Walker R. J. (1995) Carius Tube Digestion for Low-Blank Rhenium-Osmium Analysis. *Analytical Chemistry* **67**(13), 2136-2141.

Smoliar M. I., Walker R. J., and Morgan J. W. (1996) Re-Os ages of group IIA, IIIA, IVA, and IVB iron meteorites. *Science* **271**(5252), 1099-1102.

Wasson J. T. (1974) *Meteorites: Classification and Properties*. Springer-Verlag.

Wasson J. T. (1985) *Meteorites: Their Record of Early Solar-system History*. W.H. Freeman.

Wasson J. T. and Kallemeyn G. W. (2002) The IAB iron-meteorite complex: A group, five subgroups, numerous grouplets, closely related, mainly formed by crystal segregation in rapidly cooling melts. *Geochimica Et Cosmochimica Acta* **66**(13), 2445-2473.

Wasson J. T., Willis J., Wai C. M., and Kracher A. (1980) Origin of Iron Meteorite Groups IAB and IIICD. *Meteoritics* **15**(4), 385-385.